Photonic Crystal Enhanced LED for Electroluminescence Cooling

by

Zheng Li

B.S. in Physics, Peking University (2013)

Submitted to the Department of Materials Science and Engineering
and Department of Electrical Engineering and Computer Science
in partial fulfillment of the requirements for the degree of
Master of Science in Materials Science and Engineering and Master of
Science in Electrical Engineering
at the
MASSACHUSETTS INSTITUTE OF TECHNOLOGY
February 2017

Author . . . . . Signature redacted . . . .
Department of Materials Science and Engineering and Department of
Electrical Engineering and Computer Science
November 1, 2016

Certified by Signature redacted . . . .
Rajeev Ram
Professor of Electrical Engineering
Thesis Supervisor

Certified by . . . . . Signature redacted . . . .
Silvija Gradečak
Associate Professor of Materials Science and Engineering
Thesis Reader

Accepted by . . . . . Signature redacted . . . .
Donald Sadoway
Chair, Departmental Committee on Graduate Student

Accepted by . . . . . Signature redacted . . . .
Leslie A. Kolodziejski
Chair, Department Committee on Graduate Students

Photonic Crystal Enhanced LED for Electroluminescence Cooling

by

Zheng Li

Submitted to the Department of Materials Science and Engineering and
Department of Electrical Engineering and Computer Science
on January 20, 2017, in partial fulfillment of the
requirements for the degree of
Master of Science in Materials Science and Engineering and Master of Science in
Electrical Engineering

Abstract

An light-emitting diode (LED) consumes low-entropy electrical power and emits incoherent photons. In this process, the lattice heat also contributes to the output power if the LED operates at voltages below the photon energy ($qV < \hbar\omega$). Therefore, an LED can potentially cool itself, and the phenomenon is referred to as electroluminescence cooling (ELC). Although researchers recently reported LEDs with net cooling in various wavelength, the cooling power was not sufficient to compensate the heat flux from the ambient and thus no temperature drop is observed.

In this thesis, we design and fabricate a photonic crystal (PhC) enhanced unencapsulated LED for direct observation of ELC. The PhC pattern and the structure of the device are optimized to achieve approximately 76% extraction efficiency and 300 $\mu W/cm^2$ net cooling power. The LED is designed to have smaller surface area and thermal mass compared to an encapsulated one to eliminate overwhelming convection heat flux. According to our thermal models, such an LED should exhibit temperature by 0.1 K and 0.5 K in air and vacuum, respectively.

We also present preliminary fabrication processes and results. The critical steps include a flip-chip process with metal-metal bonding, substrate etching, and interference lithography for the PhC pattern.

Thesis Supervisor: Rajeev Ram
Title: Professor of Electrical Engineering

Thesis Reader: Silvija Gradečak
Title: Associate Professor of Materials Science and Engineering

Acknowledgments

First of all, I would like to thank Professor Rajeev Ram for his consistent guidance and encouragement. From him, I learned not only semiconductor physics, but also the way to think as a researcher. I also thanks Professor Silvija Gradečak for being a very supportive thesis reader.

I thank all the members in the physical optics and electronics group. I could never proceed without their generous help.

I was very fortunate to live in a community with so many friendly people here at MIT. They made me feel at home even I was in a foreign country. Particularly, I thank Yixiang for her persistent company.

Finally, my parents and grandparents have been very supportive during my life. Their unconditional love will keep motivating me to work hard in the future.

Contents

List of Figures

List of Tables

Chapter 1

Introduction

1.1 Overview

Optical refrigeration, or laser cooling, refers to cooling of macroscopic materials by anti-Stoke emission and was first theoretically investigated by Pringsheim in 1929. [10] For solid-state materials, the phenomenon was first experimentally demonstrated in rare-earth doped glasses in 1995. [11] In 2010, Seletskiy *et al.*, reported laser cooling of ytterbium doped glasses to 110 K from room temperature. [12] In 2013, Zhang *et al.* reported the first laser cooling in semiconductor. 40 K of temperature drop from room temperature was observed in CdS nanowires. [13] Similar cooling process could happen in electrically pumped solid-state materials. A forward biased light-emitting diode (LED) consumes low-entropy electrical power and pumps heat into the incoherent photon field if the LED operates at voltages below the photon energy ($qV < \hbar\omega$). [14–16] In this scenario, the wall-plug efficiency (WPE, η_{WPE}) of the LED is over 100% and net cooling might be observed. The phenomenon is called electroluminescence cooling (ELC) and has been studied for over half a century. In 1957, Tauc pointed out that the carriers diffusion in semiconductor diodes is assisted by lattice heat. [17] After Tauc's work, people build various theoretical model to study the ELC effect and the thermodynamic limitations of the energy conversion from lattice heat to optical power. [18–22] At the device level, Heikkila *et al.* reported a detailed model of ultra-efficient LEDs concerning with carrier transport, recombination and photon extraction processes. [16] According to their numerical results, a GaAs LED might generate 1 W/cm^2 of cooling power. The thermo-electrical pumping effects in LEDs of various wavelength were also observed and reported by experimentalists. [23–26] The first observation of $\eta_{WPE} > 1$ is reported in 2012 when Santhanam *et al.* used lock-in measurement tools to demonstrate an infrared GaInAsSb/GaSb LED with η_{WPE} over 200% at 135 °C. [14] In 2013, higher-than-unity η_{WPE} was achieved in mid-infrared LEDs at room temperature. [27] All these ultra-efficient LEDs operated at extremely low bias ($qV \ll kT$), and their output power densities were merely several hundreds nW/cm^2, which is not enough for direct observation of temperature drop. In order to enhance the output power, Gray *et al.* optimized the doping concentration and the active region thickness of a GaInAsSb/GaSb LED and the output power of the redesigned LED at $\eta_{WPE} = 1$ was enhanced by a factor of 621 at room temperature. [28] However, considerably higher output power is still desired to overcome the convection heat flux which is approximately 2 mW/cm^2 for a 1 K temperature difference in the air. [29] To the best of our knowledge, a direct measurement of the ELC temperature drop has not been reported.

In this thesis, we first present a comprehensive model to design an infrared LED which should exhibit ELC in Chapter 2 and 3. We achieve a cooling power of approximately $300\mu W/cm^2$ and the associated temperature drop in air is approximately 0.1 K. The first prototype of this design has been fabricated and tested. The experimental work is present in Chapter 4.

1.2 Transport and Recombination in LEDs

In this section, we review the transport and recombination processes in an LED and present the basic definition of some critical physical values.

1.2.1 Transport in LEDs

An LED is usually based on a double heterostructure, including a p doped region, an n doped region, and a sandwiched active region (AR). (Fig. 1-1) When the LED

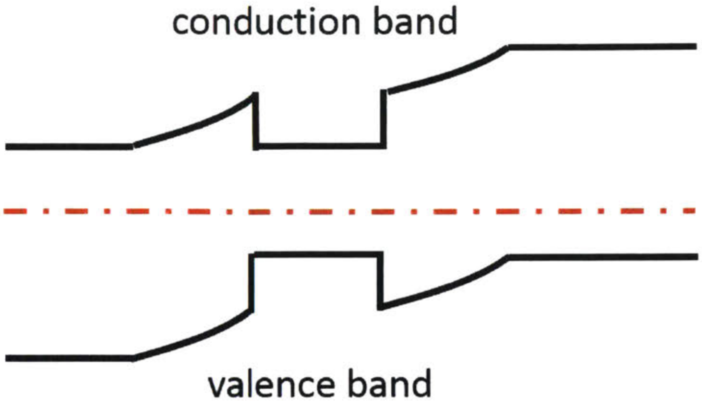

(a) Unbiased

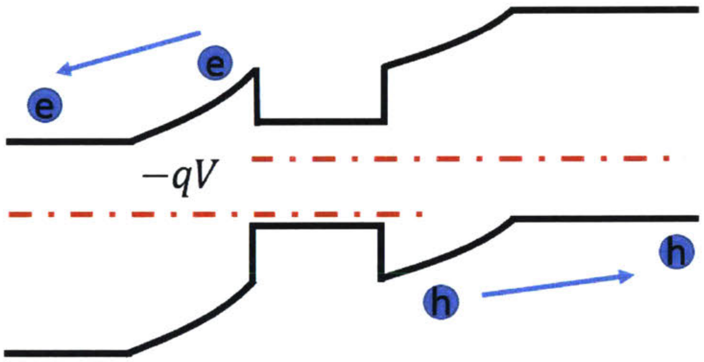

(b) Reverse biased

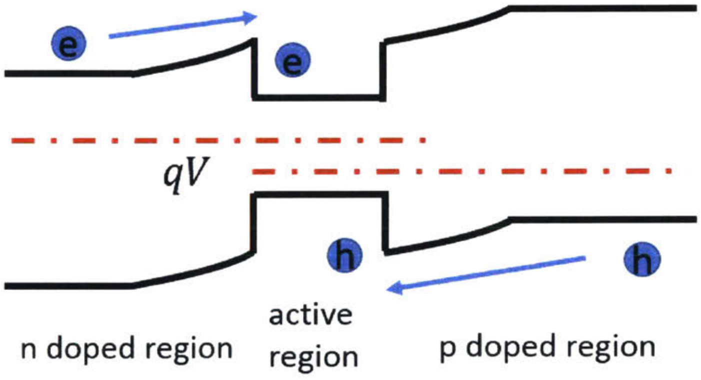

(c) Forward biased

Figure 1-1: Bandstructure of a double heterostructured LED. The red dash lines are the quasi-Fermi levels, of which the splitting represents the bias voltage. The e and h indicate electrons and holes, respectively. The blue arrows indicate the directions of the carrier transport.

is unbiased, the drift and diffusion of electrons and holes are in detailed balance due to the existence of the built-in potential barrier. Therefore, no net current nor luminescence should be observed. Fig. 1-1(a) indicates the bandsturcture in the unbiased case.

Under reverse bias, the induced electrical field is in the same direction of the built-in field and thus the diffusion current is further suppressed. (1-1(b)) The carriers are thermally generated and driven away from the AR, and no lighting should be observed. The reverse current tends to be saturated due to the limited thermal generation rate and the velocity saturation at high electrical field.

A LED usually operates under forward bias where the potential barrier is lowered and the diffusion currents dominate the transport. (Fig.1-1(c)) The electrons and holes are injected into the AR where each of the electron-hole pair has probability to recombine and the probability is defined as the injection efficiency η_{inj}.

There are three main recombination channels including Shockley-Read-Hall (SRH) recombination, bimolecular recombination and Auger recombination. Schematic plots of the mechanism of the three process are indicated in Fig. 1-2.

1.2.2 Shockley-Read-Hall recombination

The SRH recombination (Fig. 1-2(a)) is a defect-assisted process. A electron and a hole are captured by a localized defect and recombine. The energy is rapidly delivered to the phonon field and no photon is generated. The SRH recombination rate r_{SRH} takes the form [1]

$$r_{SRH} = \frac{np - n_0 p_0}{(n^* + n)\tau_h + (p^* + p)\tau_e} \tag{1.1}$$

where n (p) and n_0 (p_0) are the electron (hole) concentrations with non-zero and zero bias, respectively. τ_e (τ_h) is the time for the defect to capture a electron (hole) from the conduction (valence) band when the defect is empty (full). n^* and p^* are the electron and hole concentrations when the Fermi level were pinned at the defect energy state. At high injection regime where LEDs usually operate, we have $n \approx p \gg n_0, p_0, n^*, p^*$, and Eq. (1.1) becomes

$$r_{SRH} \approx \frac{n}{\tau_e + \tau_h} = \frac{n}{\tau_{SRH}} \tag{1.2}$$

where we define an effective SRH recombination lifetime $\tau_{SRH} = \tau_e + \tau_h$. It is also convenient to define the SRH recombination coefficient

$$A = \frac{1}{\tau_{SRH}} \tag{1.3}$$

The SRH recombination life time highly depends on the quality of the materials, the doping levels and the fabrication processes. For InGaAs materials, τ_{SRH} varies from several ns to μs.

1.2.3 Bimolecular Recombination

Bimolecular recombination is a radiative process. (Fig. 1-2(b)) A electron and a hole firstly attract each other and form a exciton due to the electrostatic force. The exiton then de-excites and generates a photon. The bimolecular recombination rate r_{bi} can be expressed as

$$r_{bi} = B(np - n_0 p_0) \tag{1.4}$$

where B is the bimolecular recombination coefficient, which mainly depends on the bandstructures of materials. For III-V semiconductors, Garbuzov has developed a relatively straightforward quantum mechanical calculation and present that

$$B = 3.0 \times 10^{-10} \frac{cm^3}{s} \left(\frac{300\ K}{T}\right)^{\frac{3}{2}} \left(\frac{E_g}{1.5\ eV}\right)^2 \tag{1.5}$$

where E_g is the bandgap and T is the temperature. [30] B of some common semiconductors are listed in Table 1.1.

Similar to the SRH case, under the high inject condition, Eq. 1.4 can be written as

$$r_{bi} \approx Bn^2 \tag{1.6}$$

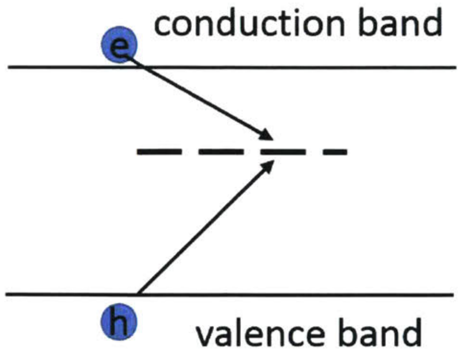

(a) Schokley-Read-Hall recombination

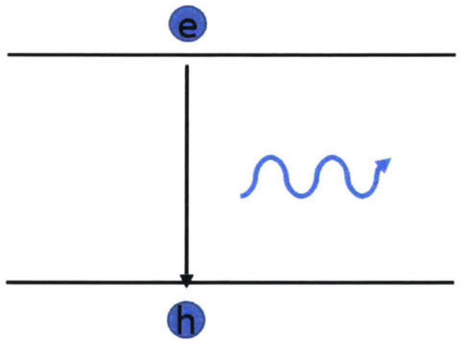

(b) Bimolecular

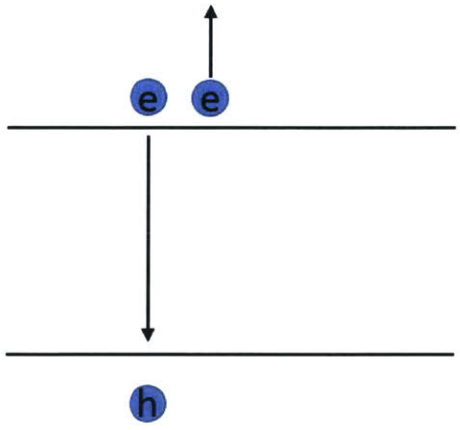

(c) Auger Recombination

Figure 1-2: The three main recombination channels in LEDs.

	E_g (eV)	B (cm^3s^{-1})
GaAs	1.42	2.0×10^{-10}
InP	1.35	1.2×10^{-10}
GaN	3.4	2.2×10^{-10}
GaP	2.26	3.9×10^{-13}
Si	1.12	3.2×10^{-14}
Ge	0.66	2.8×10^{-13}

Table 1.1: The bimolecular coefficients and bandgaps of some common semiconductors. [8]

1.2.4 Auger Recombination

Auger recombination is a non-radiative and three-body process. In Fig. 1-2(c), a electron recombines with a hole and the released energy is delivered to another electron. The second electron is knocked to a higher state and eventually thermalized by emitting several phonons. A similar process occurs with two holes in the heavy-hole (HH) subband and one electron. In this scenario, the second hole is usually knocked into the split-off (SO) or the light-hole (LH) subband. These three cases are present in Fig. 1-3. The rate of the Auger process can be empirically expressed as

$$r_A \approx C_n n^2 p + C_p n p^2 \tag{1.7}$$

where C_n and C_p describe the contributions from the CCCH and the CHHS processes, respectively. With high injection, Eq. 1.7 simplifies to

$$r_A \approx C n^3 \tag{1.8}$$

where C, as the Auger coefficient, varies from 10^{-29} to 10^{-28} cm^6/s for InGaAsP materials at room temperature. [1]

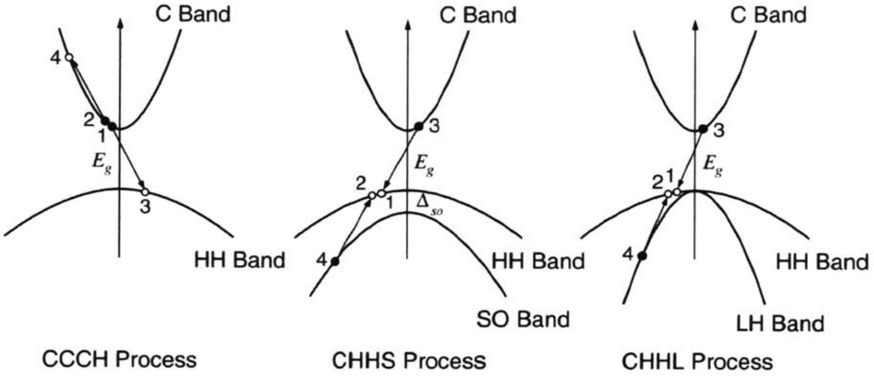

Figure 1-3: Three types of Auger processes. [1]

1.2.5 Intrinsic Quantum Efficiency

Among the three main recombination channels, only the bimolecular recombination is radiative and contributes to the output power. We define the intrinsic quantum efficiency (IQE, η_{IQE}) as the ratio of the radiative recombination rate to the total recombination rate, or, the ratio of the generated photons to the injected electron-hole pairs. According to Eq. 1.2, 1.6 and 1.8, we have

$$\eta_{IQE} = \frac{r_{bi}}{r_{SRH} + r_{bi} + r_A} \approx \frac{Bn^2}{An + Bn^2 + Cn^3} \tag{1.9}$$

It is straightforward to see IQE reaches the maximum

$$\eta_{IQE} = \frac{B}{B + 2\sqrt{AC}} \tag{1.10}$$

when

$$n = \sqrt{\frac{A}{C}} \tag{1.11}$$

Based on this fact, researchers suggest use doped AR to tune the carrier concentration. [16, 28] This is proved to be effective in thick ARs ($> 0.5\ \mu m$). However, in a thin AR and under high injection, the carrier concentration is mainly set by the cladding layer doping levels and the applied bias. As we will discuss later, in our case, a thin and intrinsic AR is preferred.

1.3 Extraction Sturctures of LEDs

In this section, we discuss the extraction issues in LEDs. Several extraction approaches are reviewed.

1.3.1 Total Internal Reflection

When an optical ray is refracted at the interface of two medium, the angles of incidence and refraction obey the Snell's law:

$$n_1 \sin\theta_i = n_2 \sin\theta_t \tag{1.12}$$

where n_1 and n_2 are the refractive indexes of the mediums on the incident and refracted sides, respectively. θ_i and θ_t are the angles of incidence and refraction. Consider the case of $n_1 > n_2$ and let $\theta_t = \frac{\pi}{2}$, the critical incidental angle

$$\theta_c = \arcsin\frac{n_2}{n_1} \tag{1.13}$$

Beyond the critical angle $\theta_i > \theta_c$, the incident rays are totally reflected and the phenomenon is referred to as total internal reflection. In an LED, the photons with incident angle smaller than θ_c are considered in the extraction cone.

The generated photons in the AR of an LED suffer from total internal reflection and usually a significant potion of the photons are trapped in the device due to the relatively high refractive indexes of semiconductor. The trapped photons will finally be reabsorbed and turn into heat because of the loss processes such as metal absorption and free carrier absorption. The extraction efficiency C_{ex} is defined as the ratio of the escaped photons to the generated ones. For example, in a planar unencapsulated LED, let $n_1 = n_{InP} \approx 3.5$ and $n_2 = n_{air} = 1$, we have $\theta_c \approx 16.6°$. Assume a point emitting source, only $C_{ex} \approx \frac{1-\cos\theta_c}{2} \approx 2\%$ of the emitted power can escape from the device. Therefore, it is critical to design extraction structures for LEDs.

1.3.2 External Quantum Efficiency and Wall-plug efficiency

Before we begin to discuss extraction structures, it is convenient to define external quantum efficiency (EQE, η_{EQE}) and wall-plug efficiency (WPE, η_{WPE}) of LEDs here.

EQE is the ratio of the escaped photons to the injected electron-hole pairs, and thus is the multiply of IQE and extraction efficiency as

$$\eta_{EQE} = \eta_{IQE} C_{ex} \tag{1.14}$$

WPE is the energy conversion efficiency. Since each electron-hole pair gains qV energy from the battery and each escaped photon on average has $\hbar\omega$ energy, we have

$$\eta_{WPE} = \frac{\hbar\omega}{qV} \eta_{EQE} \tag{1.15}$$

1.3.3 LED encapsulation

An common and effective method to overcome the extraction issue is to package the LED die with an index-matched hemispherical lens. The schematic plot is present in Fig. 1-4 where the black and blue blocks indicate the LED die and the packaging, respectively. The die is usually significantly smaller than the lens and is located at the center of the hemisphere. In this scheme, at the die/hemisphere interface, the emitted ray (red arrow) is approximately perpendicular to the hemisphere/air interface (black dash line) and thus the extraction is improved.

The state-of-the-art LEDs with proper packaging can easily have $C_{ex} > 90\%$. [26] The packing processes are also mature and widely applied in commercial LEDs. However, as we will discuss in 1.4, due to the large surface area and thermal mass of an encapsulated LED, we need eliminate the package to maximize the ELC temperature drop.

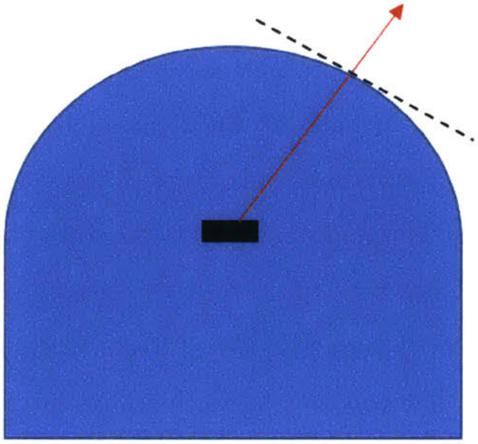

Figure 1-4: An encapsulated LED.

1.3.4 Surface Roughening

Another method to enhance the extraction is through emission surface roughening, which randomizes trajectory of the rays. As in Fig. 1-5, the blue area indicates the LED die and the red arrow is one ray trajectory. Here the top surface is the emission surface the the bottom is assumed to be reflective. If the rough feature is on the same order of the wavelength, the reflection at the top is diffusive and thus each reflected ray has certain probability to be redirected into the extraction cone after several bounces as present.

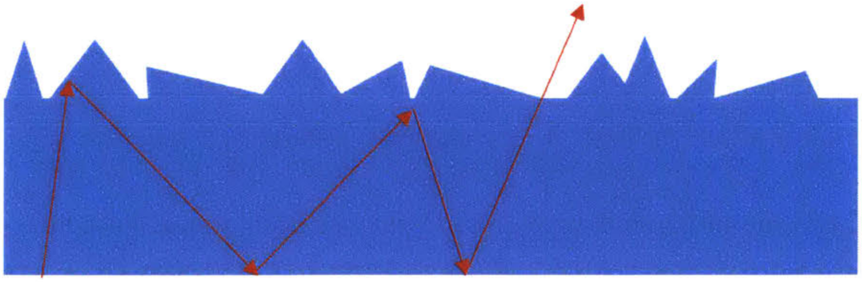

Figure 1-5: An LED with rough emission surface.

In thin-film LED technology, the epitaxial layer is usually separated from its absorbing substrate and bonded onto a metal reflector, and then the emission surface is textured. [31–34] In 1993, Schnitzer et. al. investigated the EQEs of epi-lift-off thin-film GaAs/AlGaAs LEDs with dielectric-coated Au reflectors. [33] It turned out that with a textured emission surface the EQE can be boost to 30% while the EQE is 9% for a planar surface. Rooman et. al. studied the GaInP/AlGaInP LEDs and compared the effect of using different materials between the bonded metal mirror and the epitaxial layers. [32] They concluded that the silver-loaded epoxy outperforms benzocyclobutene for doubling the achievable current while it keeps the EQE above 50%. With a very similar flip-chip and metal bonding processes in nitride material systems, [35] Haerle et. al. achieved $C_{ex} = 75\%$ for unencapsulated III-N LEDs. [34] Moreover, people also apply the surface texturing technology for volumetric LEDs with the dies usually shaped into special geometries and encapsulated, with the EQE exceeding 90%. [26,36]

1.3.5 Photonic Crystal Patterning

Another method to extract photons in LEDs is to etch photonic crystal (PhC) structure onto the emission surface. (Fig. 1-6(a)) The PhC pattern introduces periodic dielectric perturbation, and the structure can be characterized by a reciprocal lattice $\{G\}$ as

$$\epsilon(r) = \sum_G \epsilon_G \exp\left(iG \cdot r\right) \tag{1.16}$$

The modes propagating in the PhC are therefore harmonically coupled as Bloch modes

$$E(r) = \sum_G E_G \exp\left(i(k_{//} + G) \cdot r\right) \tag{1.17}$$

where $k_{//}$ in the the in-plane wavevector. When a harmonic satisfies the condition:

$$|k_{//} + G| < k_0 \tag{1.18}$$

where k_0 is the wavevector in air, it is in the extraction cone and the associated Bloch mode radiates energy into air. [37,38] (Fig. 1-6(b))

For a leaky harmonic, the in-plane wavevector is complex and thus the energy

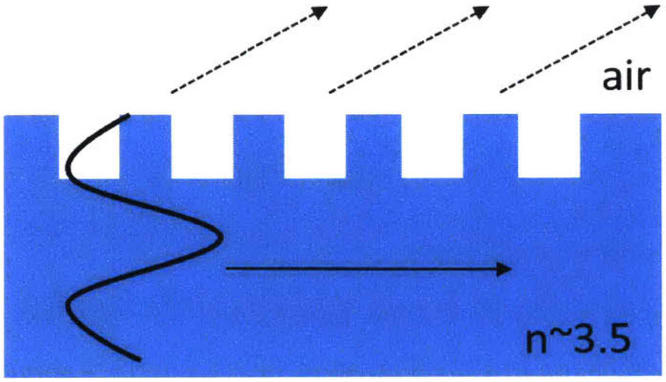

(a) PhC extraction.

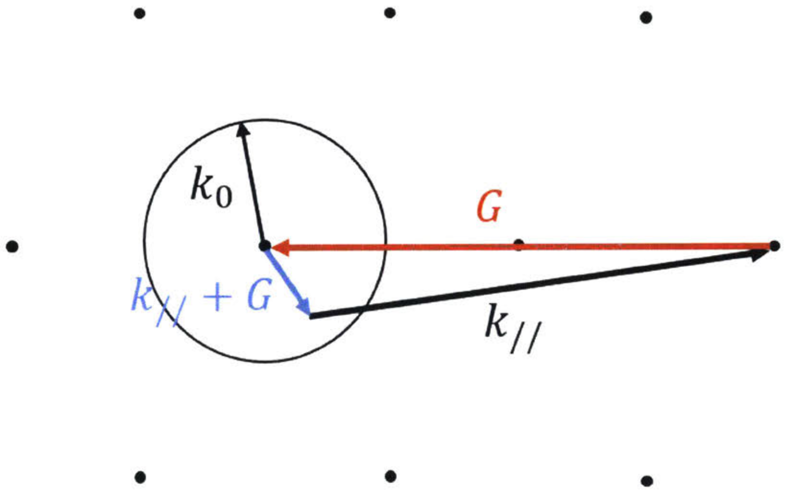

(b) Ewald construction of the extraction.

Figure 1-6: Extraction process in a PhC LED.

$I(x)$ decays exponentially as the mode propagates in the x direction as

$$I(x) = I_0 \exp(-\alpha_{ext} x) \tag{1.19}$$

where α is defined as the extraction coefficient. Usually, the extraction process competes against the absorption process such as free carrier absorption, metal absorption and band edge absorption. The extraction efficiency is determined as

$$C_{ex} = \frac{\alpha_{ext}}{\alpha_{ext} + \alpha_{abs}} \tag{1.20}$$

where α_{abs} is the absorption efficiency.

The PhC enhanced LEDs have been investigated for over two decades and are proved to be highly efficient. In 1997, Fan et al. investigated the spontaneous emission from a dipole source in a PhC slab, and the calculation showed that nearly all the light can be extracted. [39] Erchak et al. fabricated optically pumped PhC LEDs with the PhC parts not penetrating into the active regions, and found a sixfold photoluminescence intensity enhancement. [40] Wierer et al. investigated GaN LEDs with a similar PhC structure, and they claimed the LEDs could have an extraction efficiency over 70%. [41]

1.3.6 Summary and Comparison

Table 1.2 summarizes the highest measured C_{ex} of the mentioned extraction methods. The encapsulated LEDs have the best performance but are not considered as candidates for ELC due to its large surface areas. (See 1.4.) The unencapsulated LEDs have similar C_{ex}. However, the PhC patterned LEDs are more straightforward to model while the models for the distribution of photons in the surface roughened LEDs are still controversial. [37,38,42] Also, there are both theoretical and experimental work showing that PhC patterned unencapsulated LEDs have higher extraction coefficient than surface roughened LEDs. [38, 41]. Therefore, in this thesis, we will choose PhC patterned LED when it comes to unencapsulated devices.

extraction method	C_{ex}	reference
encapsulated LED	$> 90\%$	[26]
unencapsulated: textured thin film LED	75%	[34]
unencapsulated: PhC patterned LED	$> 70\%$	[41]

Table 1.2: Summary of the highest measured C_{ex} of the mentioned extraction methods.

1.4 A Thermal Model

In this section, we present a simple thermal model that drives us to the option of unencapsulated LEDs.

1.4.1 Ultra-efficient LEDs with Low Output Power

We firstly review the fact that the output power of an ultra-efficient LED is naturally low. According to Eq. 1.15, it is necessary to have

$$qV < \hbar\omega\eta_{EQE} \tag{1.21}$$

to make $\eta_{WPE} > 1$. The existence of the upper bound on the applied voltage limits the output power as well as the cooling power.

The cooling power can be expressed as

$$P_{cool} = IV(\eta_{WPE} - 1) \approx I_0 V \exp\frac{qV}{kT}\left(\frac{\hbar\omega}{qV}\eta_{EQE} - 1\right) \tag{1.22}$$

where I_0 is the saturation current of the device. If we assume η_{EQE} does not change much near the upper bound. It can be conveniently derived that the maximum cooling power is obtained at

$$V = \hbar\omega\eta_{EQE} - kT \tag{1.23}$$

which is closed to the upper bond. Therefore, the output power at $\eta_{WPE} = 1$ and the maximum cooling power both increase exponentially with η_{EQE} since the upper bound of V is proportional to EQE. For instance, Santhanam *et al.*'s LED has an

EQE of approximately 10^{-4} in the regime that $\eta_{WPE} > 1$, and the applied voltage is approximately 70 μV. [14] Therefore, the cooling power is as low as nW/cm^2.

1.4.2 Cooling in Air

An LED with over-than-unity WPE generates cooling power which competes against the heat flux from the ambient. In air, the heat flux is mainly from the air convection. According to Newton's law of cooling we have

$$C\frac{d(\Delta T)}{dt} = -P_{cool}A_{em} - h_{air}A\Delta T \tag{1.24}$$

or

$$\Delta T = -\frac{P_{cool}A_{em}}{h_{air}A}\left[\exp\left(-\frac{t}{\tau}\right) - 1\right] \tag{1.25}$$

and

$$\tau = \frac{C}{h_{air}A} \tag{1.26}$$

where ΔT is the temperature difference of the LED and the ambient. The air convective heat transfer coefficient $h_{air} \approx 2 \times 10^{-3} W/(cm^2 \cdot K)$. P_{cool} and A_{em} are the cooling power and the emission area of the die respectively. C and A are the thermal capacity and the total surface area of the LED including packing.

First we consider an encapsulated LED. The dimensions of the device and the LED die are assumed to be $0.5 \times 0.5 \times 0.5\ cm^3$ and $0.1 \times 0.1\ cm^2$, respectively. We have $A = 1.5\ cm^2$, $A_{em} = 0.01\ cm^2$. According to Eq. 1.25, if we observe 1 K temperature drop, at least we have

$$P_{cool} = \frac{h_{air}A\Delta T}{A_{em}} \approx 0.3\ W/cm^2 \tag{1.27}$$

According to Heikkila *et al.*'s model, [16] this would require that both IQE and C_{ex} are approximately unity.

In contrast, if we use an unencapsulated LED, $A \approx 2A_{em}$, and

$$P_{cool} \approx 4\ mW/cm^2 \tag{1.28}$$

which is a hundred smaller than the encapsulated case. As we will present afterward, our LED generates the maximum cooling power of approximately 300 $\mu W/cm^2$. Due to the limited cooling power and the requirement of reducing the surface area, unencapsulated LEDs are preferred for direct observation of ELC.

1.5 Thesis Overview

Chapter two presents the design of the PhC structure. We will consider four parameters of the PhC structure including the PhC hole depth, the unetched core thickness, the pitch and the filling factor. A maximum extraction coefficient of $1.5 \times 10^3\ cm^{-1}$ is obtained.

Chapter three describes our transport and the thermal models of the LED. The active region thickness is optimized to balance the optical power and the band edge absorption. We present that our LED can generate 300 μ/cm^2 cooling power.

Chapter four describes the fabrication processes of the LED.

Chapter 2

PhC structure design

In this Chapter, we optimize the PhC structure to maximize the extraction coefficient α_{ext} in Eq. 1.19.

2.1 Overview

In this section, we first describe the structure of the LED and the parameters of the PhC pattern that we optimize. The model and simulation methods are also present.

2.1.1 Structure and Parameters of the PhC Pattern

A 3D schematic figure of our LED is present in Fig. 2-1(a). The yellow, blue, green, grey and purple blocks indicate gold, n-InP, InGaAs, p-InP and InP handle, respectively. The epi layers are based on the InGaAs/InP material system, with the InGaAs layer as the active region. The device is n-up and the upper surface is the emission surface where the triangular PhC pattern is etched. The gold p contact, which is also the back reflector, is formed between the InP handle and the p cladding layer through metal-metal bonding. The detailed fabrication process will be reviewed in Chapter 4.

A plot of the cross-section is present in Fig. 2-1(b) and the parameters of the PhC structure are also defined. We consider four parameters in our design: the hole depth t, the unetched core thickness t, the pitch of the holes p and the filling factor f. Note that here the filling factor is defined as the portion of the air volume.

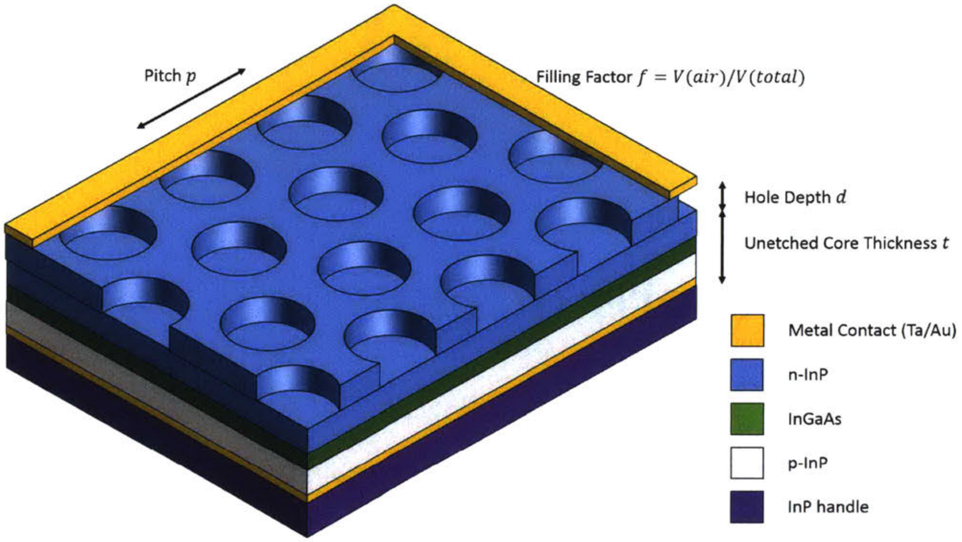

(a) A 3D schematic figure of the LED.

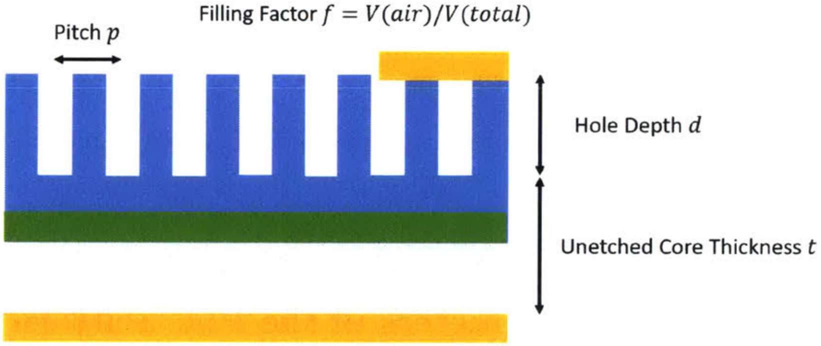

(b) Cross-section of the LED.

Figure 2-1: Schematic plot the LED and the definition of the parameters.

2.1.2 Models and Simulation Methods

We employ a 3D finite-difference time-domain (FDTD) engine to compute α_{ext}. A PhC patterned dielectric slab with the refractive index $n \approx 3.5$ is applied to model the LED. The thickness of the slab is $t + d$, and the length in x and y are fixed at 9 μm. Above the slab, 3 μm of air is set to separate the extraction structure and the boundaries. The meshing of the simulation is 50 nm. At the bottom of the slab we set the boundary condition to be perfectly reflective while perfectly matched layers (PMLs) are used for the other five boundaries.

A emitting dipole is placed at the center of the unetch part of the slab and the spectrum is Gaussian with $\lambda = 1550\ nm$ and $\Delta\lambda = 100\ nm$. The dipole orientation is in the $x - y$ plane because TE-like modes have stronger coupling with the conduction band to heavy hole subband transition in a thin AR. [1]

Around the dipole, five sensors are defined to record the integrated flux trapped in the slab. Each sensor is a square box without top and bottom and centered at the dipole. The height of the sensors is the same as the slab thickness. In the $x - y$ plane, the length of the five sensors are $4\mu m$, $5\mu m$, $6\mu m$, $7\mu m$ and $8\mu m$. The flux passing through each sensor is integrated and the FDTD simulation operates for enough long time. We employ the integrated flux of each sensor as the $I(x)$ in Eq. 1.19, with x= $2\mu m$, $2.5\mu m$, $3\mu m$, $3.5\mu m$ and $4\mu m$. Specifically, according to Eq. 1.19, we have

$$I_i \approx I_0 \exp\left(\alpha_{ext} x_i\right) \tag{2.1}$$

where $i = 1, 2, 3, 4, 5$ and I_i is the integrated power of the ith sensor. Since x_i and I_i are known, linear regression can be applied to extract α_{ext}. A snapshot of the field evolving is present in Fig. 2-2. The yellow squares and the arrow indicate the positions of the sensors the dipole respectively. The blue circles indicate the PhC holes. The inset plot present the fitting of $I(x_i)$ in log scale and good linearity is observed.

We have also varied the dipole frequency and compute the output efficiency using our FDTD simulation to compare with Fan *et. al*'s work. [39]. We present the simulation benchmark of our model against Fan *et. al*'s work in Fig. 2-3 where the left and right figures are from our model and Fan's model, respectively. We observe similar similar values and trend from these models.

As we discuss above, t, d, p and f are considered as parameters in our design. However, a global optimization is extremely consuming and thus we decouple these parameters to achieve a local optimum.

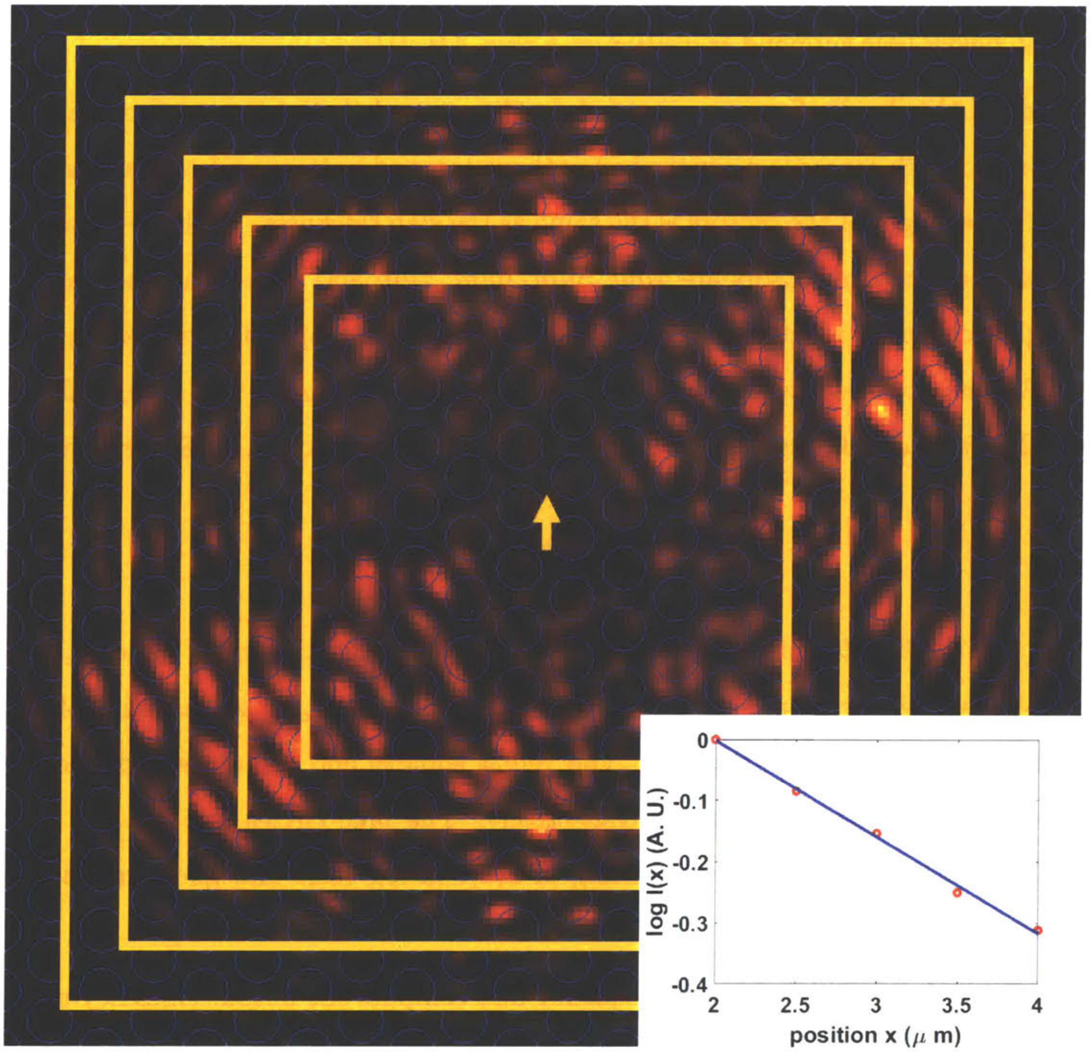

Figure 2-2: A example of the field evolving and fitting of α_{ext}.

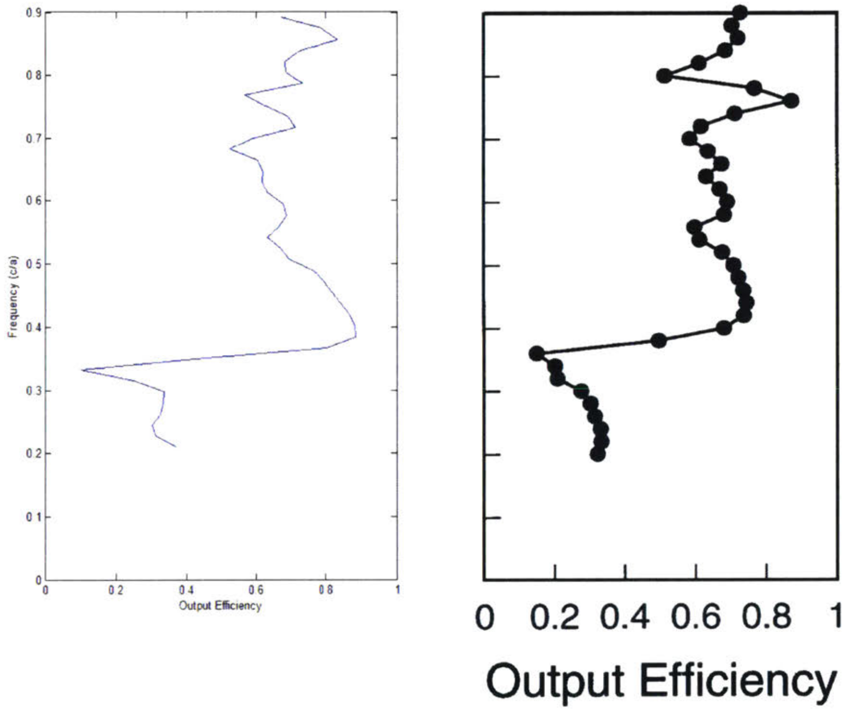

Figure 2-3: Simulation benchmark against Fan *et. al*'s work.

2.2 Optimize t and d

In this section, we focus on the optimization of the hole depth d and unetched core thickness t.

2.2.1 General Considerations

The first fact we need to consider is that the etch depth affects the number of the guided modes. According to extraction requirement of a given guided mode (Eq. 1.18), if t is so thick that the LED supports many guided modes, it will be difficult to construct a PhC pattern to satisfy Eq. 1.18 for all the modes. Therefore, t needs to be kept small enough to ensure there are only a few guided modes supported.

A small t squeezes a guided mode into the PhC region and the extraction is enhanced because the overlap between the evanescent tail and the PhC becomes larger. In [37], it is present that α_{ext} roughly satisfies

$$\alpha_{ext} \propto t^{-3} \tag{2.2}$$

as long as the guided mode is well confined in the unetched core and the epi layer thickness is fixed.

However, it is still necessary to keep t above a certain value. First, if the holes penetrate the AR, the output power will decrease since it is proportional to the volume of AR, and defects such as dangling bonds will be introduced into the AR. Second, several guided modes have to be confined in the unetched core to ensure reasonably large overlap with the AR, otherwise the transition rates will be significantly suppressed. Therefore, as will be present afterward, in our simulations, we keep $t > \frac{\lambda}{2n_{core}}$, which guarantees that as least the fundamental mode is well localized in the unetched core.

Another fact we have to take into account is the resonance effect within the PhC region and the unetched core. Each layer can be considered as a microcavity since the thickness is on the same order of the wavelength. Similar to the resonance-cavity LEDs (RCLEDs) when t or d satisfy the resonance condition, local maximum and minimum of extraction should be observed. [8,37,43–46] The oscillation can be utilized to achieve an enhanced extraction coefficient.

2.2.2 Simulation results

In Fig. 2-4, we present the plot of α_{ext} versus t and d. Here we fix $p = 1.2\ \mu m$ and $f = 0.5$. First, as we stated above, we keep $t > 250\ nm$, and within this regime a small t is generally preferred for extraction. The oscillation of α_{ext} with t and d can also be observed and the maximum in the simulation region is $\alpha_{ext} \approx 1.2 \times 10^3\ cm^{-1}$ at $t = 0.27\ \mu m$ and $d = 0.39\ \mu m$. The maximum satisfies the resonance condition of $2(n_{InP}t + n_{PhC}d) \approx \frac{5}{2}\lambda$ and $2n_{PhC}d \approx \frac{3}{2}\lambda$, where $n_{InP} \approx 3.5$ and $n_{PhC} = \sqrt{n_{InP}^2(1-f) + n_{air}f} \approx 2.57$ are the (effective) refractive index of the core and PhC region, respectively.

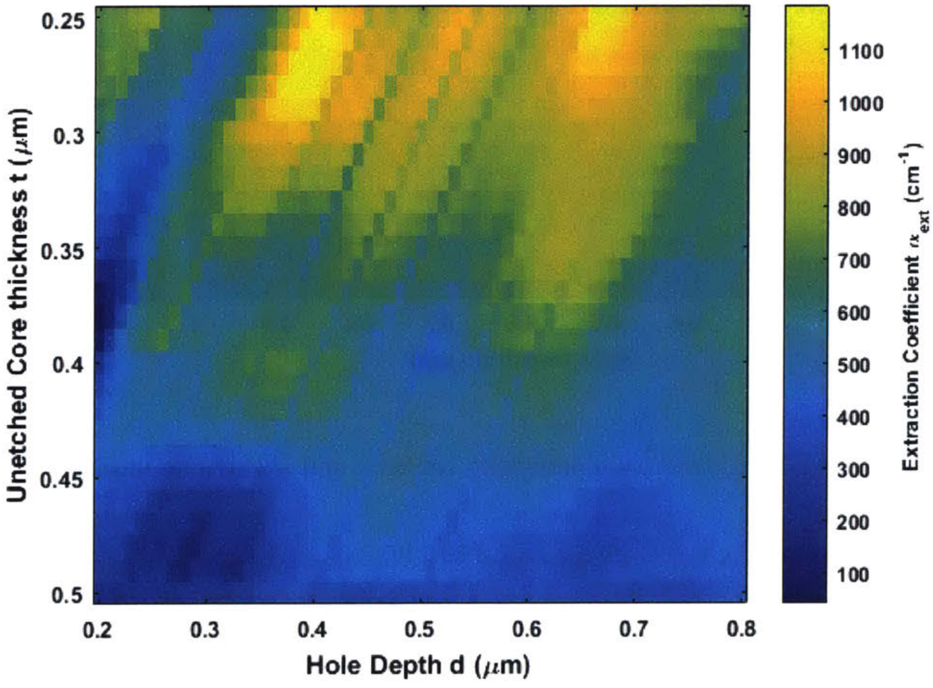

Figure 2-4: Extraction coefficient versus t and d (3D FDTD simulation).

We also present a 2D model of α_{ext} versus t and d in Fig. 2-5 to confirm the resonance does take place in our case. The 2D model is based on an 1D grating waveguide and we utilize the coupling mode theory to compute the diffraction mode and the associated extraction. A similar simulation can be referred to [45]. Due to the vanishing -1 Fourier component of 1D gratings with $f = 0.5$, in the 2D model we apply $f = 0.3$ while $p = 1.2\ \mu m$ is unchanged. In Fig. 2-5, the solid and dash line indicate $2(n_{InP}t+n_{PhC}d) \approx \frac{2N+1}{2}\lambda$ and $2n_{PhC}d \approx \frac{2N+1}{2}\lambda$. As expected, the maximum extraction points approximately locate at the intersections of the solid and the dash lines.

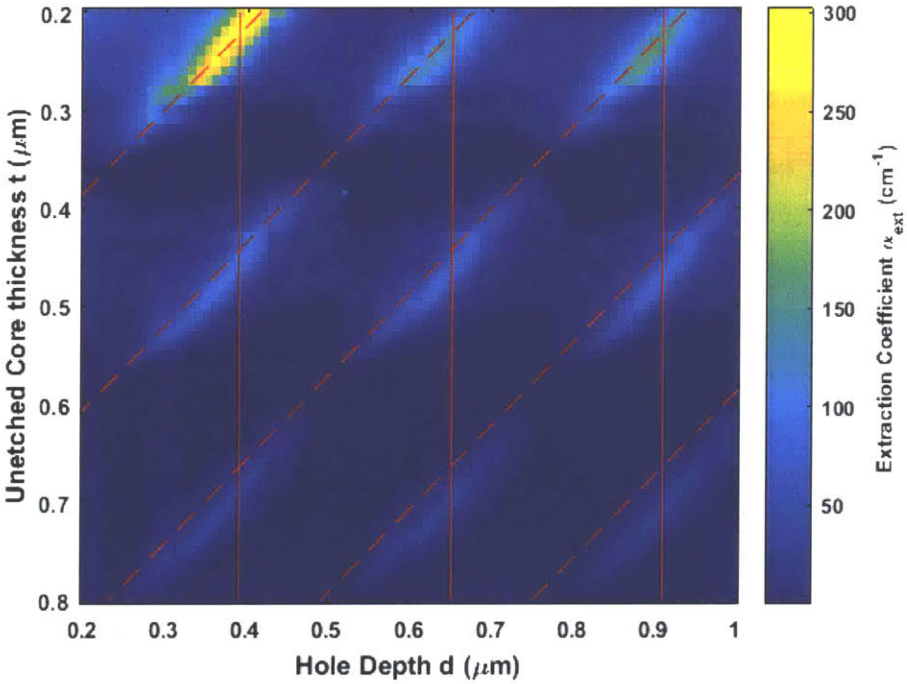

Figure 2-5: Extraction coefficient versus t and d (2D simulation).

Form now on, we fix $t = 0.27\mu m$ and $d = 0.39\ \mu m$ and vary other parameters.

2.3 Optimize p

2.3.1 General Considerations

The norm of a Fourier vector is inversely proportional to p. In Fig. 2-6 we indicate the first three Fourier vector of hexagonal lattice and their norms are

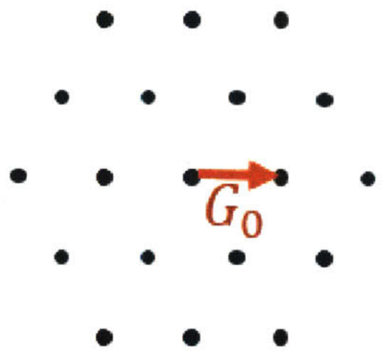

(a) Hexagonal lattice G_0.

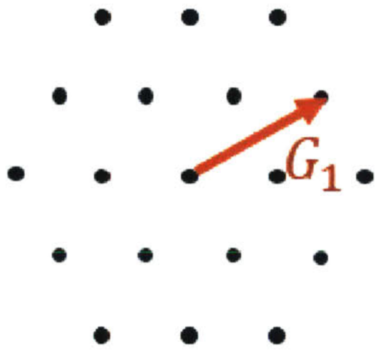

(b) Hexagonal lattice G_1.

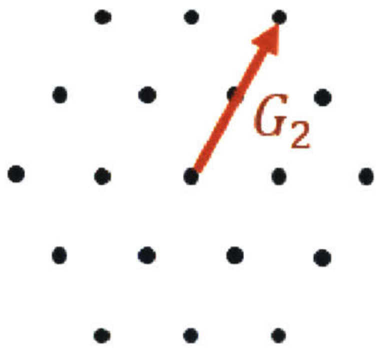

(c) Hexagonal lattice G_2.

Figure 2-6: The first three Fourier vector of hexagonal lattice.

$$|G_0| = \frac{4\pi}{\sqrt{3}p} \tag{2.3}$$

$$|G_1| = \frac{4\pi}{p} \tag{2.4}$$

$$|G_2| = \frac{8\pi}{\sqrt{3}p} \tag{2.5}$$

Eq. 1.18 states the requirement of extraction for G and $k_{//}$. For simplicity, we consider the fundamental mode, which usually carries most of the optical energy, and let $k_{//} = \beta$. Usually $\beta \approx nk_0$ is several times larger than k_0, and thus the feasible G is within a small range around β. Therefore, we expect the optimum G satisfies

$$|G| \approx |\beta| \tag{2.6}$$

. The vector addition can be referred to Fig. 1-6(b).

Since t, d and f determine β, as we vary p, α_{ext} should reach maximum when Eq. 2.6 satisfies for associated G. Note that it is possible that several Gs contribute to the extraction, and the peaks of α_{ext} may merge with each other.

2.3.2 Simulation results

We fix $t = 0.27\ \mu m$, $d = 0.39\ \mu m$ and $f = 0.5$ in the 3D FDTD mode, and present the α_{ext} versus p plot in Fig. 2-7. Two relative peaks of $\alpha_{ext} \approx 1.5 \times 10^3\ cm^{-1}$ and $\alpha_{ext} \approx 1.2 \times 10^3\ cm^{-1}$ are observed at $p' \approx 0.74\ \mu m$ and $p'' \approx 1.2\ \mu m$, respectively. To verify that Eq. 2.6 satisfies, we use the 2D model we mentioned in Sec. 2.2 to compute the fundamental mode profile. (See Fig. 2-8.) $\beta \approx 2.9k_0$ is also obtained from the model. Let $|G_{0,1,2}| = \beta$, according to Eq. 2-6, we have $p_0 \approx 0.6\ \mu m$, $p_1 \approx 1.1\ \mu m$ and $p_2 = 1.3\ \mu m$. It is straightforward to verify that $p' \approx p_0$ and $p'' \approx \frac{p_1+p_2}{2}$. Therefore, as expected, at the first peak, the main contribution to extraction is from G_0 and the contribution from G_1 and G_2 merge with each other at the second peak. Since the extraction at the first peak is the higher one, we will set $p = p' = 0.74\ \mu m$ afterward.

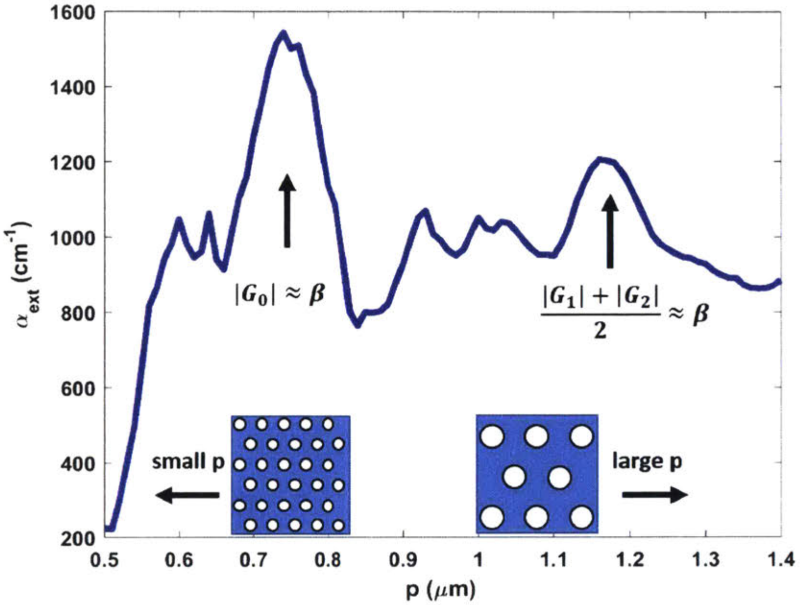

Figure 2-7: Extraction coefficient versus pitch of the lattice (3D FDTD simulation).

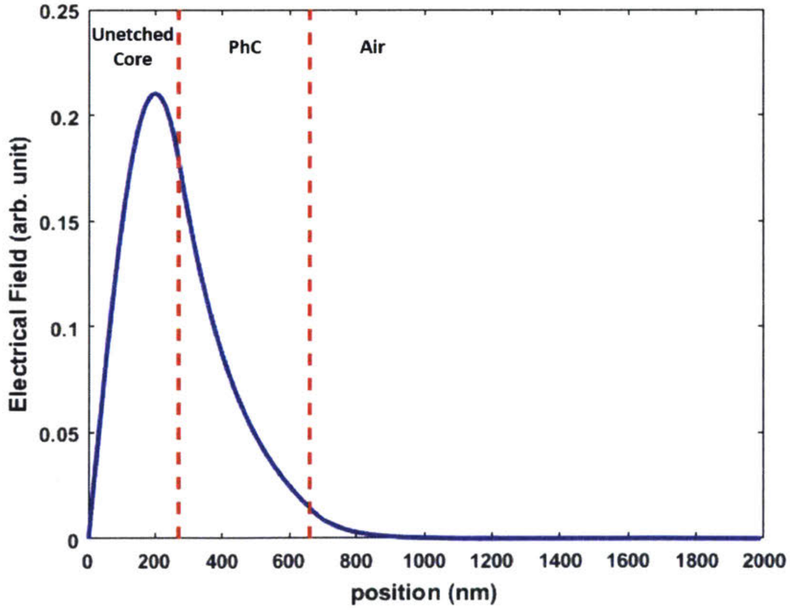

Figure 2-8: Fundamental mode profile. (2D simulation)

2.4 Optimize f

2.4.1 General Considerations

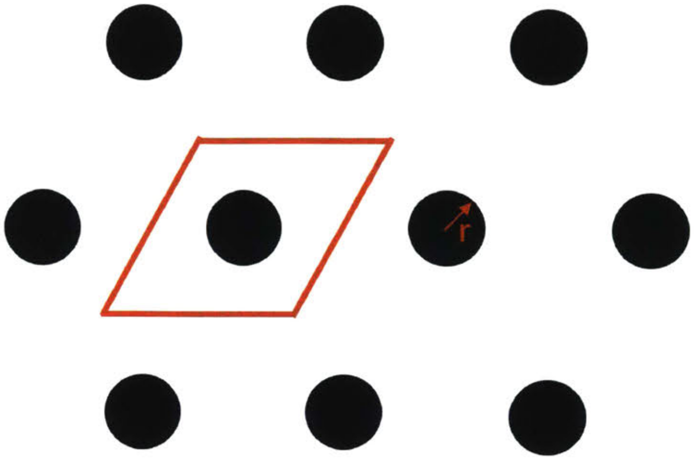

Figure 2-9: Fourier integral on hexagonal lattice.

As a simple estimation, the extraction coefficient of a given G is proportional to the square of the Fourier strength of the dielectric perturbation $(\Delta\epsilon(G))^2$. [37] The filling fact mainly affect the Fourier strength of the PhC. When $f \to 0$ and $f \to 1$ the Fourier strength should vanish because the perturbation no longer exists in these cases. Consider the Fourier integral of a function $f(x, y)$ on hexagonal lattice in Fig. 2-9, where the value of the function is 1 in the black circular region and is zero elsewhere. We perform the integral with in a unit cell which is indicated by the red lines as

$$F(G) = \frac{1}{A}\int_{circle} dS \exp(iGr) = \int_0^r rdr \int_0^\pi d\theta \left(\cos(|G|r\cos\theta) - i\sin(|G|r\cos\theta)\right) \tag{2.7}$$

where A is the area of the unit cell and r is the radius of the circle.

First perform integral over θ and then over r, and consider the definition of Bessel functions

$$F(G) = \frac{2\pi}{A}\int_0^r rdrJ_0(|G|r) = \frac{2\pi rJ_1(|G|r)}{A|G|} \tag{2.8}$$

where J_0 and J_1 are the zeroth and first order Bessel function of the first kind.

According to Eq. 2.8, as $f \rightarrow 0$ or $r \rightarrow 0$, $F(G) \rightarrow 0$. However, the behavior of $f \rightarrow 1$ is less obvious here. Since we assume the the circles in Fig. 2-9 are non-overlapping, $f \rightarrow 1$ is actually not applicable. We can develop some general ideas by investigating the properties of Bessel functions. Bessel functions of the first kind oscillate and the amplitudes decrease, and thus as r increases $J(|G|r)$ generally decreases. This lead to the vanishing of $F(G)$ when r is large.

2.4.2 Simulation Results

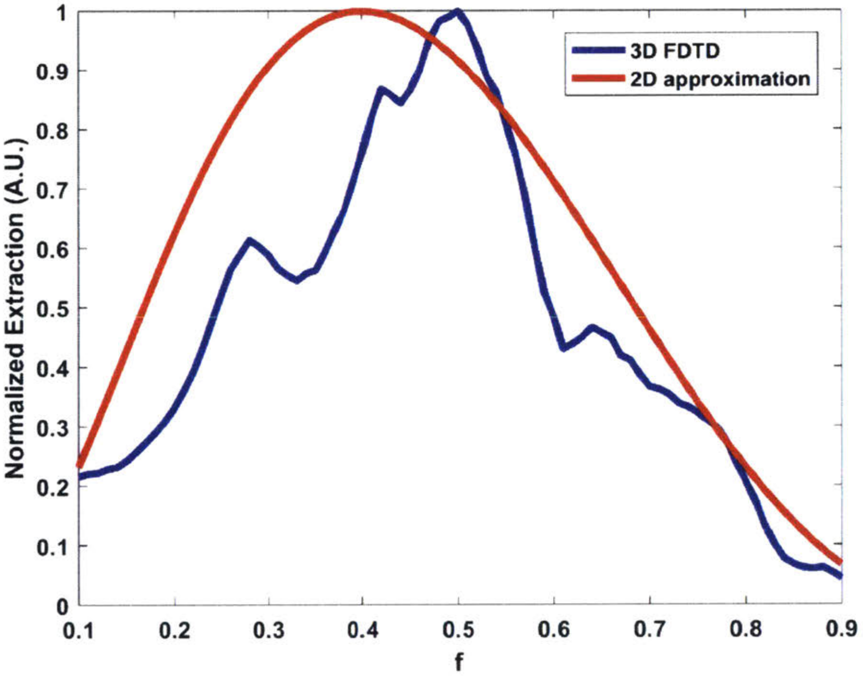

Figure 2-10: Extraction coefficient versus f.

In Fig. 2-10, we present the α_{ext} versus f plots from both the 3D FDTD simulations and the 2D estimation we mentioned above. The extraction coefficients here are normalized by their maximum values to have clearer comparison. As expected, the extraction coefficients from both models vanish as $f \rightarrow 0$ and $f \rightarrow 1$. The values are also comparable. However, the optimum fs are 0.4 and 0.5 for 2D and 3D models, respectively. The deviation may come from the fact that in the 2D model we only consider G_0 but G_1 and G_2 also have contribution to the extraction. Another difference of the two plots is that the plot of 3D FDTD simulations has several local peaks, which might be also due to the contribution from high order Fourier vectors. As the 3D FDTD simulations suggest, we set $f = 0.5$ afterward.

2.5 Conclusion

In this chapter, we review the design of our PhC in detail. We perform 3D FDTD simulations to compute the extraction coefficients and several 2D models are also employed to verify the physical pictures. The optimal parameters are $t = 0.27\ \mu m$, $d = 0.39\ \mu m$, $p = 0.74\ \mu m$ and $f = 0.5$. The maximum extraction coefficient is $\alpha_{ext} = 1.5 \times 10^3\ cm^{-1}$.

We conclude the sensitivity of our parameters. Let $\alpha_{ext} > 1.35 \times 10^3\ cm^{-1}$, which corresponds to 10 % of relative error, the fabrication tolerance of t, d, p and f are approximately 18%,13%,14% and 10% respectively according to Fig. 2-4,2-7 and 2-10.

We also point out the estimation of C_{ex} through Eq. 1.20 is relatively conservative. According to our simulation, approximately 10% of the emitting energy is directly coupled into the extraction cone instead of the guided modes. These escaped energy is not considered in our design.

Chapter 3

Transport and Thermal Models

In this chapter, we present the transport and thermal models of our device. We firstly investigate the layer stacking and absorption processes and their effect on the extraction efficiency. The active region thickness is optimized to achieve the maximum cooling power. We also compute the maximum temperature drop in air and vacuum.

3.1 Layer Stacking

The hole depth $d = 390\ nm$ and the unetched core thickness $t = 270\ nm$ are fixed according to the optical design. We have to further consider the thickness of the p cladding, the AR and the n cladding within the unetched core. Some general considerations are addressed as follows. First, the cladding layers have to be thick enough (usually $> 150\ nm$) to effectively spread the current and provide stable mechanical support. Second, near metal contact, people apply thin ($\approx 10\ nm$) heavily doped layers to enhance electrical conductance. As for t_{AR}, on one hand, thick AR is preferred because the output power is approximately proportional to the volume of the AR, or t_{AR}. On the other hand, the effective band edge absorption increases with t_{AR}.

We propose the layer stacking and the doping profile in Fig. 3-1. The heavily doped metal contact layers are $10\ nm$ and $2 \times 10^{18}\ cm^{-3}$ doped. We fix the p cladding layer as $150\ nm$ and n cladding layer is then $110\ nm - t_{AR}$. The doping of the p cladding, the n cladding as well as the PhC region are $1 \times 10^{17} cm^{-3}$. The AR

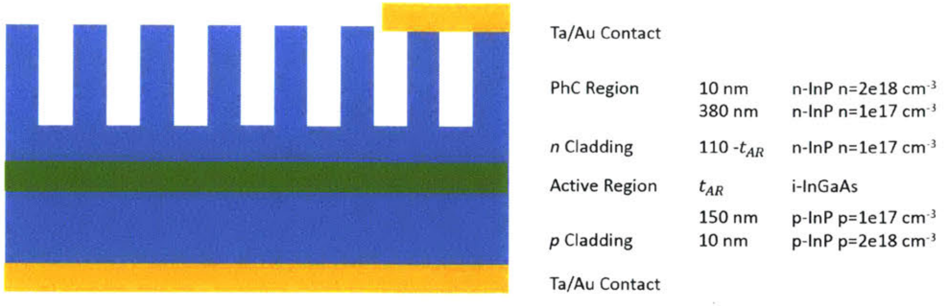

Figure 3-1: Proposed layer stacking.

remains intrinsic. Our AR differs from the suggestion of using doped AR from some researcher. [16, 28] According to Eq. 1.9, it is possible to enhance IQE by tuning the carrier concentration in the AR. However, for thin ARs as in our device, the carrier concentrations in the ARs are mainly set by the cladding layers and thus doping AR does not help. We simulate the IQEs of devices with doped and intrinsic ARs and present the results in Fig. 3-2. In Fig. 3-2(a), $t_{AR} = 1\ \mu m$, and the blue and red lines indicate the doped and intrinsic AR, respectively. We observe that the IQE is enhanced for the device with doped AR. However, in Fig. 3-2(a), with $t_{AR} = 0.1\ \mu m$, no obvious enhancement is observed. Also, in real devices, to introduce dopants may increase the defect density and the non-radiative recombination rate. Therefore, we use intrinsic ARs for our device design.

3.2 Absorption Processes

According to Eq. 1.20,

$$C_{ex} = \frac{\alpha_{ext}}{\alpha_{ext} + \alpha_{abs}}$$

we need compute the effective absorption to obtain the extraction efficiency. Therefore, we review the absorption processes in this section.

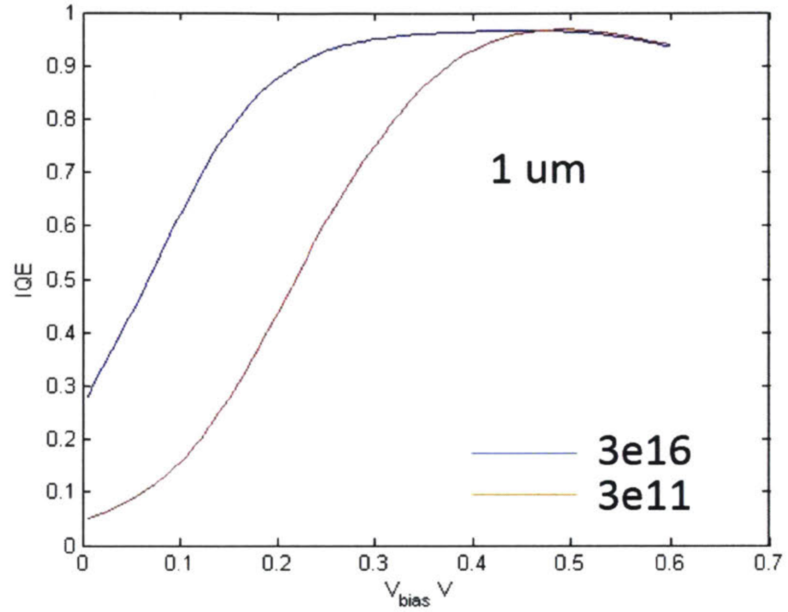

(a) IQEs in devices with 1 *um* ARs.

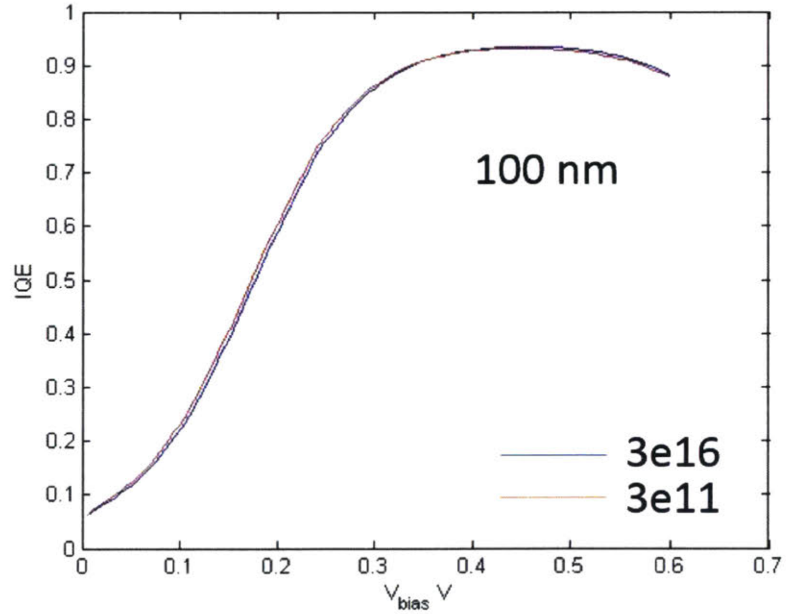

(b) IQEs in devices with 100 *nm* ARs.

Figure 3-2: Comparison of doped and intrinsic ARs.

3.2.1 Free Carrier Absorption

Free carrier absorption (FCA) is a intraband process and usually assisted by phonons. [47] Consider a electron in the conduction band absorbs a photon and is excited to a higher energy state. Since the momentum of the photon is negligible, a phonon is usually emitted to compensate the momentum difference of the two electron states. Similar processes can be observed for holes in the valence band. Such processes are irreversible.

Fig. 3-3 and Fig. 3-4 present the experimental data of FCA coefficient $\alpha_{FC,n}$ and $\alpha_{FC,p}$ for n-InP and p-InP, respectively. In Fig. 3-3, the electron concentrations are 1) $4 \times 10^{16} cm^{-3}$, 2) $2 \times 10^{17} cm^{-3}$ and 3) $4 \times 10^{17} cm^{-3}$. As will be present afterward, we will apply $10^{17} cm^{-3}$ doping for both the n-InP and p-InP cladding layers. Therefore, both coefficients are smaller than 5 cm^{-1}.

3.2.2 Band-edge Absorption

Band-edge absorption (BEA) can be considered as the reverse process of bimolecular recombination: a photon with energy above the bandgap excites a electron-hole pair. This process is reversible since the electron-hole pair has certain probability to go through radiative recombination and emit another photon. This phenomenon is referred to as photon recycling and mainly happens in ARs of LEDs and lasers. [48–50]

Fig. 3-5 presents the experimental data of BEA coefficient α_{be} of 1550-InGaAs at 297 K. For photons near the InGaAs bandgap, α_{be} is relatively sensitive to the photon energy. On average, we have $\alpha_{be} \approx 6 \times 10^{3}$ cm^{-1}.

Since BEA mainly happens in the AR, the effective BEA coefficient α'_{be} depends on the AR thickness t_{AR} as

$$\alpha'_{be} = \alpha_{be} \frac{\int_{AR} I(z)dz}{\int I(z)dz} \tag{3.1}$$

where $I(z)$ is the angular averaged intensity profile in the vertical direction. The integrals in the numerator and denominator are performed over the AR and the device, respectively. The core of our device, where most of the optical power trapped,

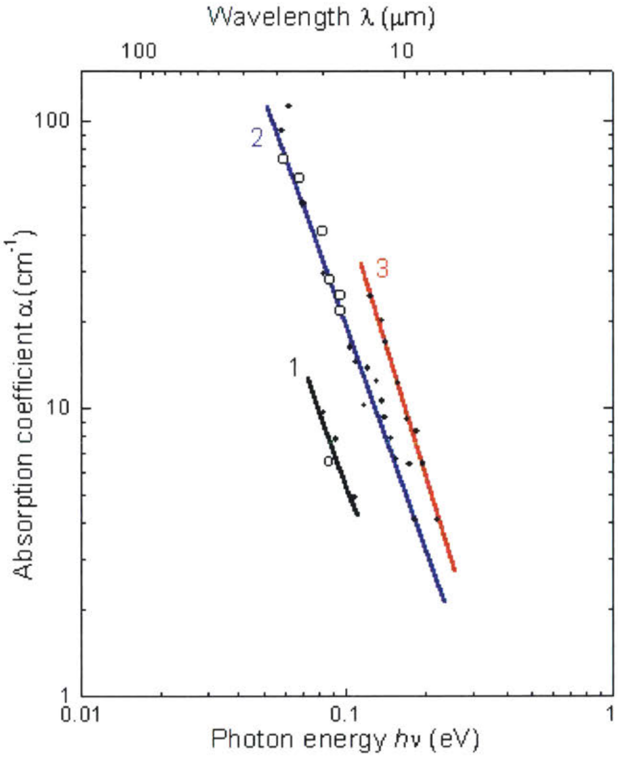

Figure 3-3: FCA coefficient of n-InP versus photon energy at 300 K. [2]

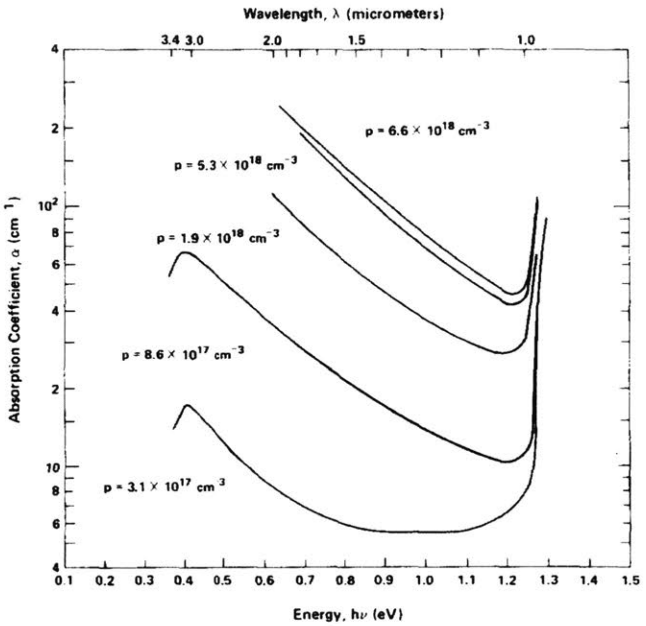

Figure 3-4: FCA coefficient of p-InP versus photon energy at 297 K. [3]

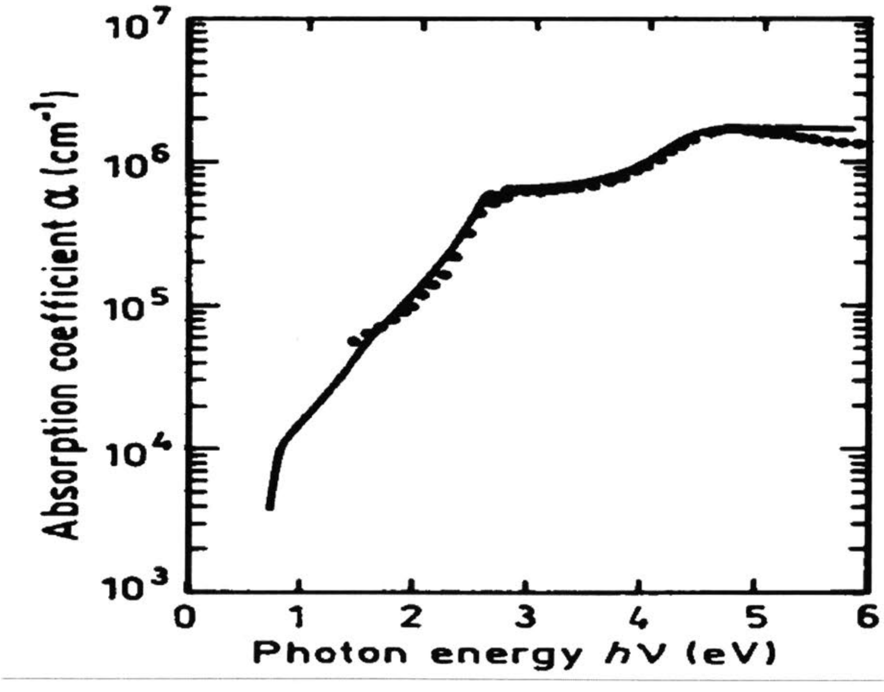

Figure 3-5: BEA coefficient of 1550-InGaAs versus photon energy at 297 K. [4]

has thickness $t = 0.27\ \mu m$. As will be present afterward, t_{AR} is a few tens of nm, Therefore, α'_{be} is approximately a few hundreds of nm.

3.2.3 Metal Absorption

Metal contact of the device also contribute to irreversible absorption. For a slab waveguide on a metal reflector the absorption coefficient depends on the (complex) refractive index of metal and the waveguide core. [51]

We used the mode solver of RF module in COMSOL to simulate the metal loss for the fundamental TE mode in this structure. We calculated the complex propagation constant at 1550 nm by using the complex refractive index of gold $n_{Au} = 0.5831 + 9.8640i$ and tantalum $n_{Ta} = 0.86 + 8.43i$ at this wavelength and a refractive index of 3.5 for the unetched core and an effective index of 2.57 for the PhC. [52] The evanescent tail in the metal leads to metal loss. The estimated propagation loss in this structure is $\alpha_m \approx 355\ cm^{-1}$. The mode profile of the fundamental TE mode is present in Fig. 3-6.

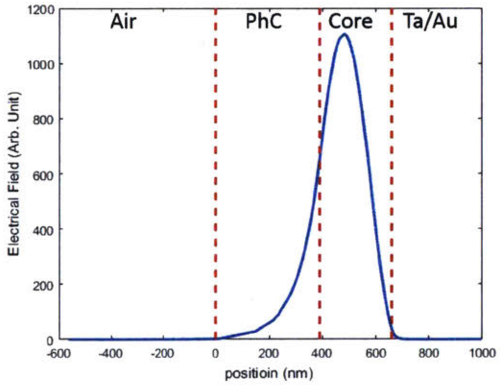

Figure 3-6: Fundamental TE mode with absorptive Ta/Au mirror.

3.2.4 Comparison and Discussion

As discussed above, α'_{be} and α_m is as least ten times larger than α_{FC} in our device. Therefore, we will only use $\alpha_{abs} = \alpha'_{be} + \alpha_m$ to estimate the absorption processes and optimize t_{AR}.

3.3 Transport Models and AR Thickness design

We have demonstrated that BEA and metal loss dominates absorption processes in our device. Since BEA depends on t_{AR}, we will optimize t_{AR} via our transport models in this section.

3.3.1 Models and Simulation Flow

We will vary t_{AR} to search for the maximum cooling power. Before that, we describe our models and simulation flow. For a given t_{AR}, we firstly extract the intensity profile in the device from our FDTD simulation and compute α'_{be} according to Eq. 3.1. C_{ex} is then obtained from Eq. 1.20 by letting $\alpha_{abs} = \alpha'_{be}$ and $\alpha_{ext} = 1.5 \times 10^3\ cm^{-1}$.

The transport and recombination processes are simulated by SimWindows, which is an 1D finite element solver of the drift-diffusion equation. [53]

The model utilizes the recombination rate equations of carriers (Eq. 1.1, 1.4, 1.7) to determine the spontaneous emission rate and IQE. The SRH, bimolecular, and Auger recombination coefficients are $A = 4.5 \times 10^5\ s^{-1}$, $B = 1.46 \times 10^{-10}\ cm^3 s^{-1}$ and $C = 9 \times 10^{-29}\ cm^6 s^{-1}$, respectively. These numbers are referred to Gfroerer *et al.*'s work on a LED of similar structure. [54] At this step, the $I - V$ curve and the IQE curve are obtained. The output power $L = IV\eta_{IQE}C_{ex}$ and the cooling power $P_{cool} = L - IV$ are then computed as a function of V. Let $max_V\left(P_{cool}\left(t_{AR}, V\right)\right) = P_m(t_{AR})$, which is the maximum cooling power for a given t_{AR}. We vary t_{AR} and repeat the simulations and then the optimum t_{AR} associated with the maximum P_m is obtained. The simulation flow is present in Fig. 3-7.

3.3.2 Simulations Results

We first present a benchmark (L-I plot) of Simwindows simulations against experiments in Fig. 3-8. Here the experimental data is from an unpackaged ELC-1550

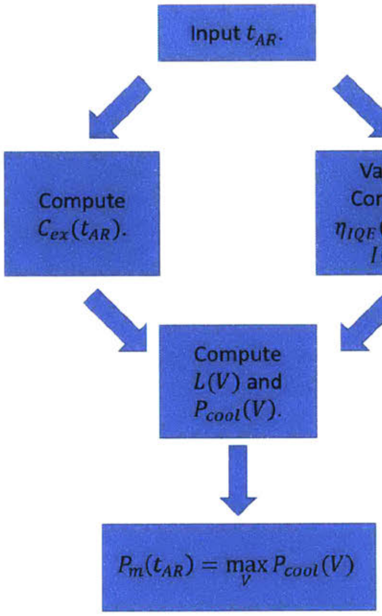

Figure 3-7: Simulation flow.

LED die, which is based on InGaAs/InP material multiple quantum wells. As can be observed, the simulation results have the same trend as the experiments at various temperature. Note that the curves are vertically shifted by approximately $10^2\times$ because we assume unity extraction and collection in the simulations.

We present the angular averaged intensity profile in the vertical direction from our FDTD simulations in Fig. 3-9. Note that the profile is not purely TE-like due to the fact that the dipole emission has TM-like component. The C_{ex} and $alpha'_{BE}$ versus t_{AR} plot is present in Fig. 3-10. As expected, C_{ex} decreases with t_{AR}. In Fig. 3-11, we present P_m versus t_{AR}. As we have discussed, the non-monotonic dependence of P_m on t_{AR} is due to the competition of extraction and total AR volume. Here the optimum point is at $t_{AR} \approx 5\ nm$ and $P_m \approx 300\ \mu/cm^{-3}$. According to Fig. 3-10, this indicates $C_{ex} \approx 76\%$.

For the optimum t_{AR}, we present the $L-I$ and $P_{cool}-I$ plots in Fig. 3-12. We can observe that the output power at $\eta_{WPE} = 1$, or $P_{cool} = 0$, $L_{\eta=1} \approx 0.015\ W/cm^2$. This value is 10^6 higher than that in [28]. We achieve this significant enhancement of performance because our device has $C_{ex} \approx 76\%$ and thus it works at higher applied

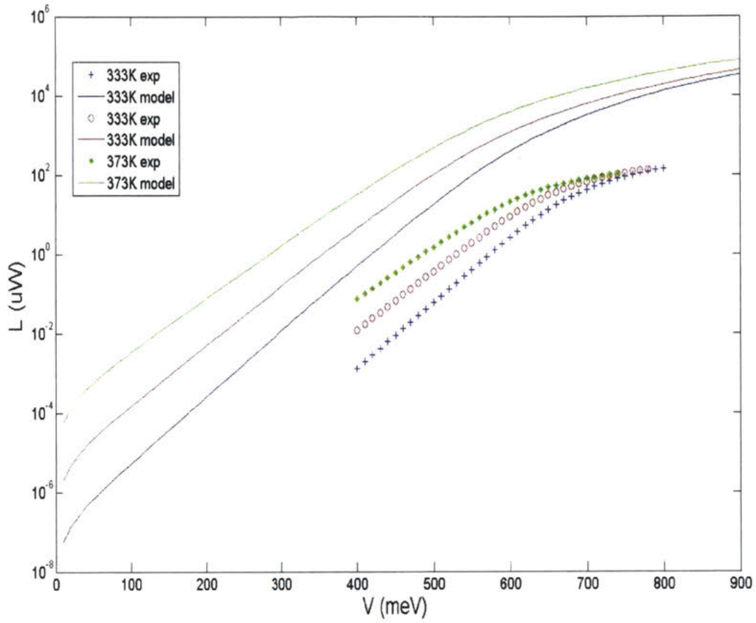

Figure 3-8: Benchmark of Simwindows simulations against experiments.

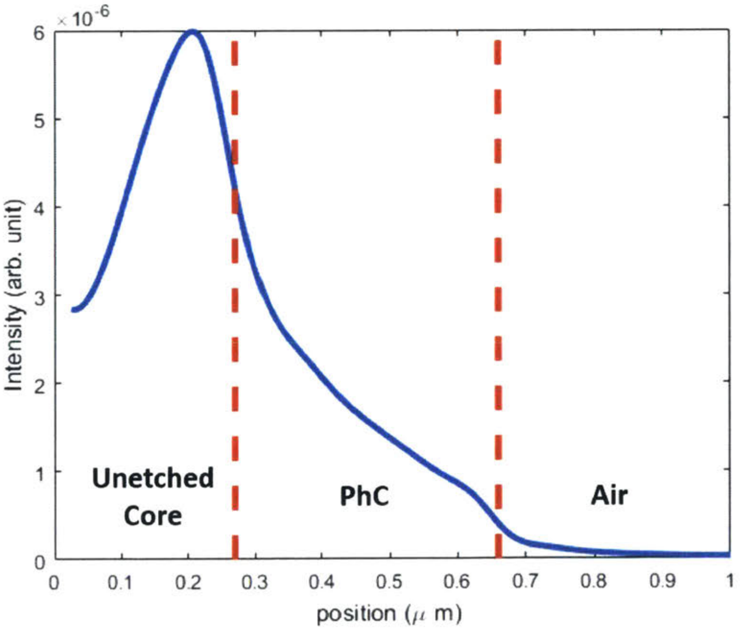

Figure 3-9: Angular averaged intensity profile in the vertical direction.

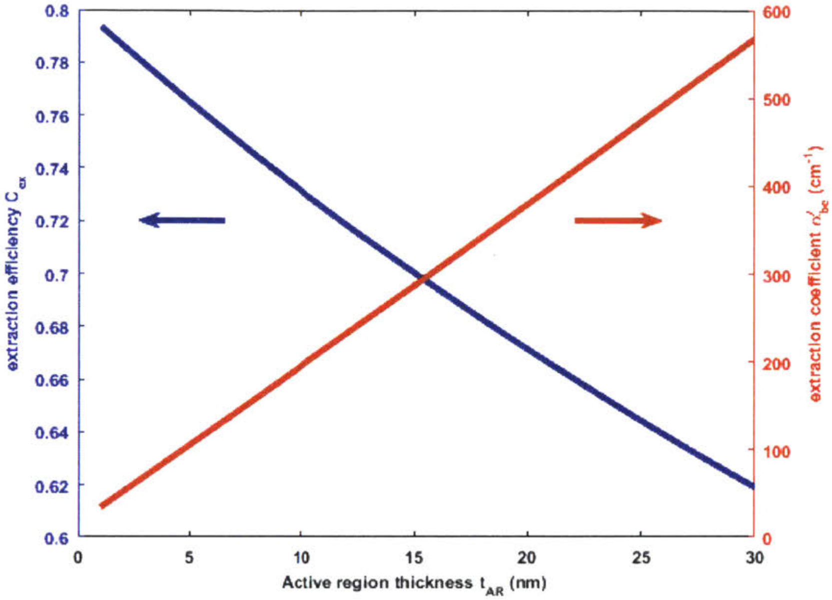

Figure 3-10: Extraction coefficient versus AR thickness.

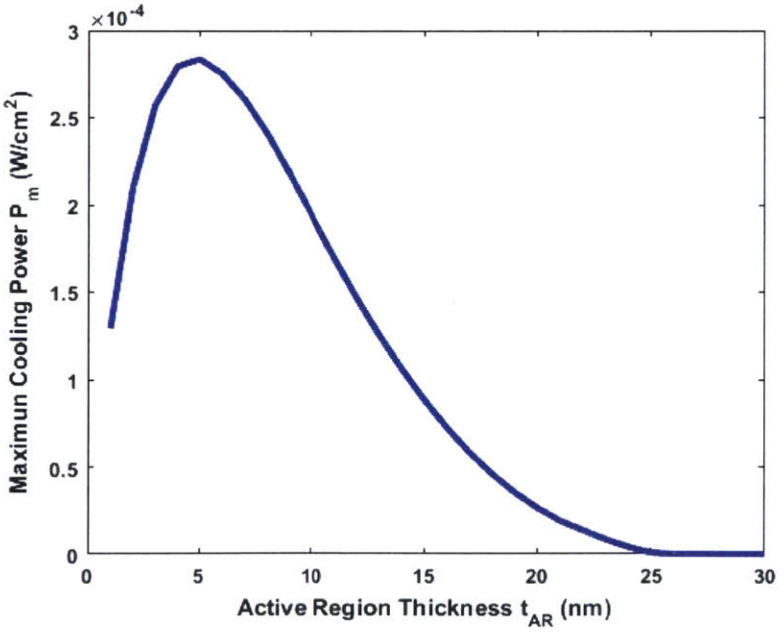

Figure 3-11: Maximum cooling power versus AR thickness.

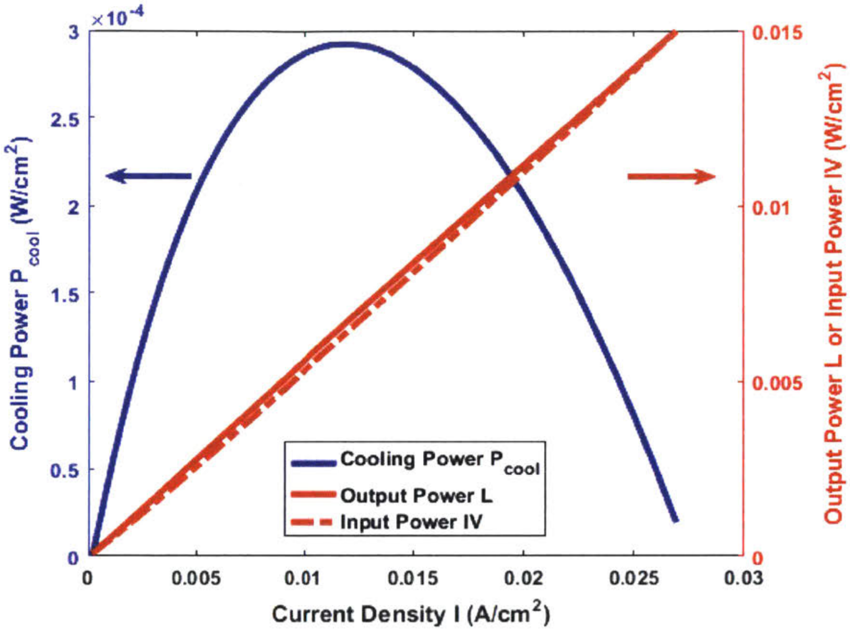

Figure 3-12: Output power and cooling power versus current density.

voltage $\frac{qV}{\hbar\omega}$, compared to 0.05 in Gray *et al.*'s work. Also, note that our device is unencapsulated and the area can be easily enlarged to cm^2 without complex packaging. Therefore, we can expect mW of total output power, which can be of practical use.

Fig. 3-10 and 3-11 also indicate that the fabrication tolerance of t_{AR} is relatively large. Even we double the optimal t_{AR} as $t_{AR} = 10\ nm$, we still obtain $C_{ex} \approx 73\%$ and $P_{cool} \approx 100\ \mu/cm^2$.

3.4 Thermal Models

We have optimized the device structure and determined that the maximum cooling power $P_{cool} \approx 300\ \mu/cm^2$. In this section, we evaluate the temperature drop of the device. The parameters we will use are listed in Table 3.1.

	sign	value	comment
LED density	ρ_d	$4.8\ g/cm^3$	
LED length	l_d	$0.1\ cm$	
LED thickness	t_d	$200\ \mu m$	handle included
LED specific heat	c_d	$0.31\ J/(g\ K)$	
LED thermal conductivity	k_d	$0.68\ W/(cm^2\ K)$	
Air convection coefficient	h_{air}	$2 \times 10^{-3}\ W/(cm^2\ K)$	[29]
Wire length	l_w	$0.5\ m$	
Wire radius	r	$100\ \mu m$	
Wire specific heat	c_w	$0.38\ J/(g\ K)$	
Wire density	ρ_m	$8.9\ g/cm^3$	
Wire electrical resistivity	ρ_e	$10^{-5}\ \Omega \cdot cm$	
Wire thermal conductivity	k_w	$0.48\ W/(cm^2\ K)$	
Cooling power	P_{cool}	$300\ \mu/cm^2$	maximum cooling
LED current density	I_d	$0.01\ A/cm^2$	See Fig. 3-12
Wire current density	I_w	$0.3\ A/cm^2$	$I_w = I_d \frac{l_d^2}{\pi r^2}$

Table 3.1: Parameters in our thermal models.

3.4.1 Cooling in Air

The thermal model in air has already been discussed in Section 1.4.2. For unencapsulated LEDs, $A \approx 2A_{em}$ and Eq. 1.25 becomes

$$\Delta T = \frac{P_{cool}}{2h_{air}} \left[\exp\left(-\frac{t}{\tau}\right) - 1 \right] \tag{3.2}$$

with the time constant

$$\tau = \frac{\rho_d t_d c_d}{2h_{air}} \approx 7.44\ s \tag{3.3}$$

and maximum cooling

$$\Delta T_m = -\frac{P_{cool}}{2h_{air}} \approx -0.1\ K \tag{3.4}$$

We present the $T - t$ plot in Fig. 3-13. The temperature drop can be easily measured by simple setups such as thermocouples.

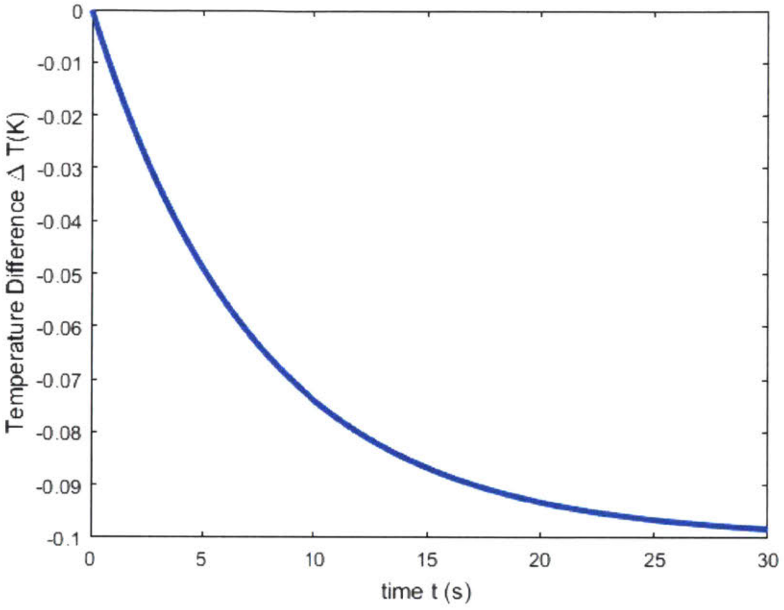

Figure 3-13: Cooling process in air.

3.4.2 Cooling in Vacuum

A more dramatic temperature drop should be observed if we put the LED into a vacuum chamber to eliminate the air convection. We propose to use the electrical wires as mechanical support of the LED. The proposed setup is present in Fig. 3-14. In this scenario, the cooling has to compete against the heat flux from the wire. The heat sources are the Joule heat generated and the chamber which is thermalized with the ambient.

The temperature distribution $T(x, t)$ along the wire satisfies

$$\rho_m c_w \frac{\partial T}{\partial t} = I_w^2 \rho_e - \frac{k}{l_w} \frac{\partial^2 T}{\partial x^2} \tag{3.5}$$

At $x = 0$ and $x = l_w$ the wire is connected with the chamber and the LED, respectively. The boundary conditions are thus

$$T|_{x=0} = T_0 \tag{3.6}$$

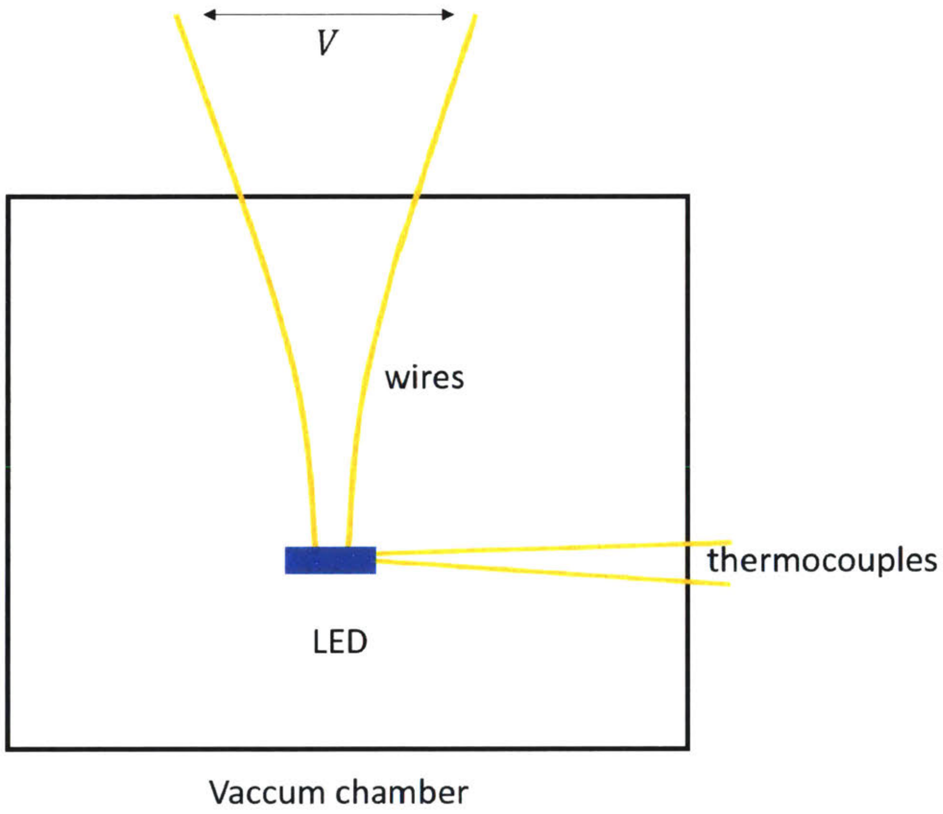

Figure 3-14: Proposed setup to measure cooling in vacuum.

and

$$\pi r^2 k_w \frac{\partial T}{\partial x}\bigg|_{x=l_w} = -\frac{1}{2} P_{cool} l_d^2 \tag{3.7}$$

where $T_0 = 300\ K$ is the ambient temperature. The prefactor $\frac{1}{2}$ exists because two wires are symmetrically connected to the LED. Note that in Eq. 3.7, we assume the thermalization of the LED is much faster than the wires because the thermal conductance of the wires K_w is much smaller than that of the LED K_d since

$$\frac{K_d}{K_w} = \frac{k_d}{k_w}\frac{l_d^2}{\pi r^2}\frac{l_w}{t_d} \approx 10^5 \tag{3.8}$$

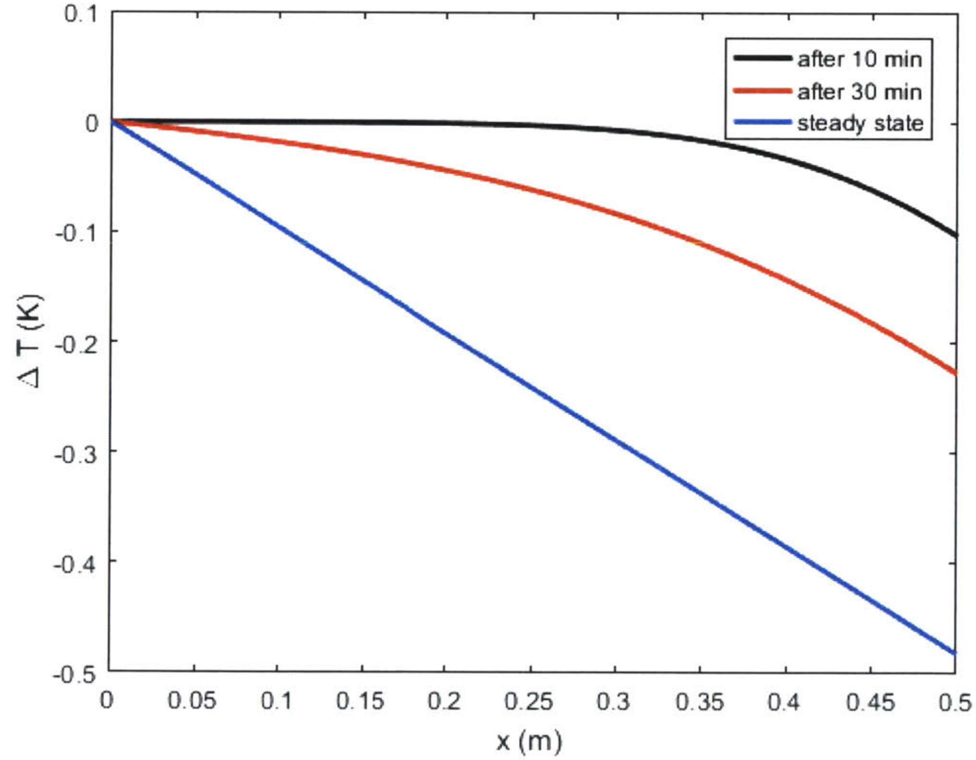

Figure 3-15: Cooling process in vacuum.

In Fig. 3-15 we present the cooling process in vacuum. The temperature drop at the LED end of the wire is 0.1 K and 0.2 K after 10 min and 30 min, respectively. For the steady state, the temperature drop is approximately 0.5 K.

Chapter 4

Fabrication and Related Issues

We have discussed the design of our devices in the previous chapters. Critical components of the device include a metal back reflector, PhC extraction structure of approximately cm^2 large and a grid-shape top contact. In order to realize these devices, we developed a fabrication recipe. In this chapter, we review each fabrication step and present the related issues.

4.1 Epitaxial Layer Stacking

MBE samples were grown by our collaborators from Lincoln Lab. The layer stacking is presented in Fig. 4-1. Note that the layer stacking is different from our optimum design suggested in the last chapter because the growth request is based on one of our previous designs. The main difference is that the active region of the MBE wafer is thicker (60 nm) compared to 5 nm in the design. The thicker active region leads to higher band edge absorption and the simulated extraction coefficient is less than 50%. However, this difference should not have any effect on the fabrication processes.

Our collaborators also provide us with a lattice matched InGaAs calibration sample. (Fig. 4-1) The InGaAs layer is around 3000 A with a thin InP cap on top of it. In the following section, without specific indications, each process step is preformed on the calibration wafer. In the final section, we also present the fabrication results on the device epitaxial samples.

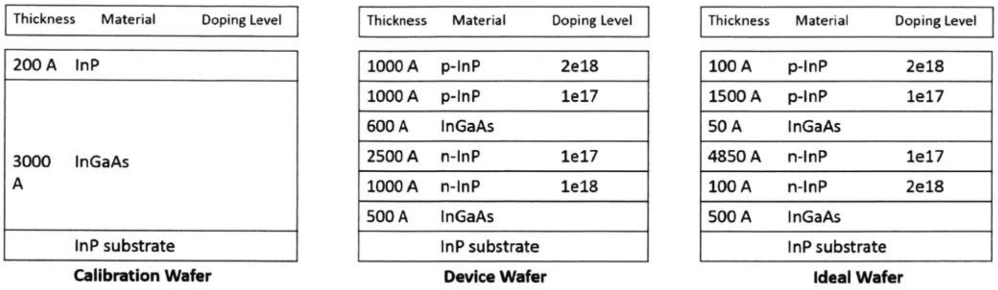

Calibration Wafer

Thickness	Material	Doping Level
200 A	InP	
3000 A	InGaAs	
	InP substrate	

Device Wafer

Thickness	Material	Doping Level
1000 A	p-InP	2e18
1000 A	p-InP	1e17
600 A	InGaAs	
2500 A	n-InP	1e17
1000 A	n-InP	1e18
500 A	InGaAs	
	InP substrate	

Ideal Wafer

Thickness	Material	Doping Level
100 A	p-InP	2e18
1500 A	p-InP	1e17
50 A	InGaAs	
4850 A	n-InP	1e17
100 A	n-InP	2e18
500 A	InGaAs	
	InP substrate	

Figure 4-1: The layer stacking of the device wafer, the calibration wafer and our ideally designed wafer.

4.2 Fabrication Process

A table of the detailed fabrication process can be found in Appendix. In this section, we briefly describe each step schematically and present the associated photos.

4.2.1 Deposition and Bonding

The first step of our fabrication flow is thermal compression bonding, which is widely used in CMOS technologies for wafer scale bonding. [55] In this process, we deposit metal films onto two wafers that are to be bonded, and apply force to bring the two metal-coated surfaces into contact. Usually, the bonded sample is kept at an elevated temperature for a certain period. [9] In this period, inter-diffusion of metal atoms happens and the interface gradually disappears. This process generates a solid mechanical bond as well as good electrical conductivity. [56]

The most frequently used metals in thermal compression bonding are Cu, Al, and Au due to their high diffusion rates. [9, 57] Compared with Au, Cu and Al are softer and thus they yield better ductile properties. However, both Cu and Al films require extensive preparation, such as formic acid vapor cleaning, before bonding because a surface oxide forms immediately after deposition. [9] This step can usually be skipped for gold.

The applied pressure and elevated temperature are selected to ensure a reasonably fast and stable diffusion process. Typical settings for 200 *mm* wafers are present in

metal	applied force	temperature	time	pressure
Al	$> 70\ kN$	$400 - 450\ °C$	$20 - 45$ min	$> 2\ MPa$
Au	$> 40\ kN$	$260 - 450\ °C$	$20 - 45$ min	$> 1\ MPa$
Cu	$20 - 80\ kN$	$380 - 450\ °C$	$20 - 60$ min	$0.5 - 2\ MPa$

Table 4.1: Typical settings for 200 *mm* wafers. [9]

Table 4.1 The applied pressure is usually from 1 to 10 MPa to plastically deform the metal film. This can effectively decrease the bow and warp of the surfaces. [58] High uniformity of the pressure is desired, which lowers the requirement of the total force as well as the stress gradients in the film. The bonding temperature is usually from $250 - 400\ °C$. The elevated temperature accelerates the thermal-asstisted diffusion process. Also, high temperature lowers the required applied pressure. [59] This is desired because high pressure leads to increased potential of damaging the sample. However, it is usually challenging to equalize the thermal expansion of the two wafers under such high temperature. [9] Therefore, precise alignment of the wafers and good control of the thermal ramp is required. [55, 58]

In our process, the epitaxial wafer is first cleaved into small pieces of approximately $0.5\ cm \times 0.5\ cm$. Mechanical grade InP is also cleaved into pieces which are larger than the epitaxial ones in order to make the bonding process easier. Ti/Pt/Au of $100/1000/2000A$ metal layers are then deposited on all pieces through ebeam deposition. Here Ti is an adhesion layer and Pt is the diffusion blocking layer. These layers induce extra metal loss and lower the extraction efficiency and will be replaced by Ta/Au, which is less lossy, in our future work. After the deposition, each epitaxial wafer piece is bonded with InP piece through Au-Au bonding process in a EV501 machine. The bonding temperature and applied pressure are 300 $°C$ and 4 MPa, respectively. Here the samples is heated from the room temperature to 300 $°C$ in approximately 15 min. The bonding process lasts for 60 min. In the same machine, the samples go through an annealing process with the same temperature and pressure for another hour to enhance the bonding quality. After the annealing, if the bonding of the two pieces are stable under slight push, it is considered successful. However, this test may not be sufficient because the bonding could fail in the following step.

For example, in our previous recipe, the contact metal layer is chosen as Zn/Au due to the lower contact resistance of Zn/InP. [60] However, the epitaxial layer buckled and broke after wet etching under this condition. We have fixed the recipe by applying Ti/Pt/Au contact because Ti is much harder than Zn and serves as a better mechanical supporting layer. Furthermore, Pt layer prevents the Au from diffusing into InP and shorting the diode junction during the bonding process.

A schematic plot of these processes is present in Fig. 4-2. Photos of top view and side view of a bonded calibration sample are in Fig. 4-3 and Fig. 4-4, respectively.

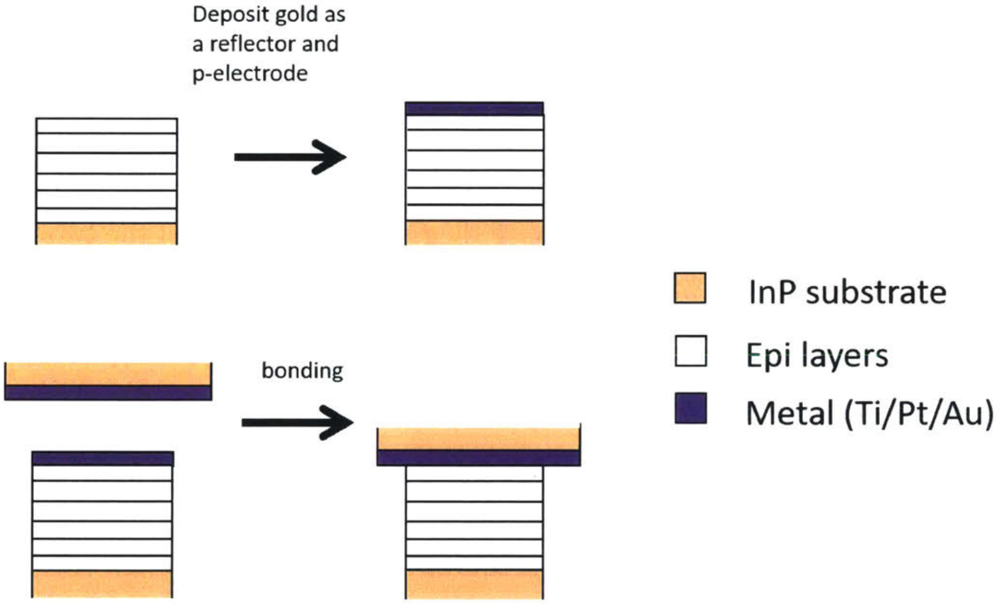

Figure 4-2: A schematic plot of the deposition and bonding processes.

4.2.2 Wet Etching of InP Substrate

HCl:H_2O is an extensively used etching system for InP with InGaAs etch stop. [61,62] The etching mechanism of InP in HCl solution can be schematically present as in Fig. 4-5. [5,6] The reaction starts with a synchronous exchange of bonds (k_1). In this step, H-Cl and InP bonds break and In-Cl and P-H bonds form. The process happens when molecular HCl contact with the InP surface and is considered as the rate limiting step.

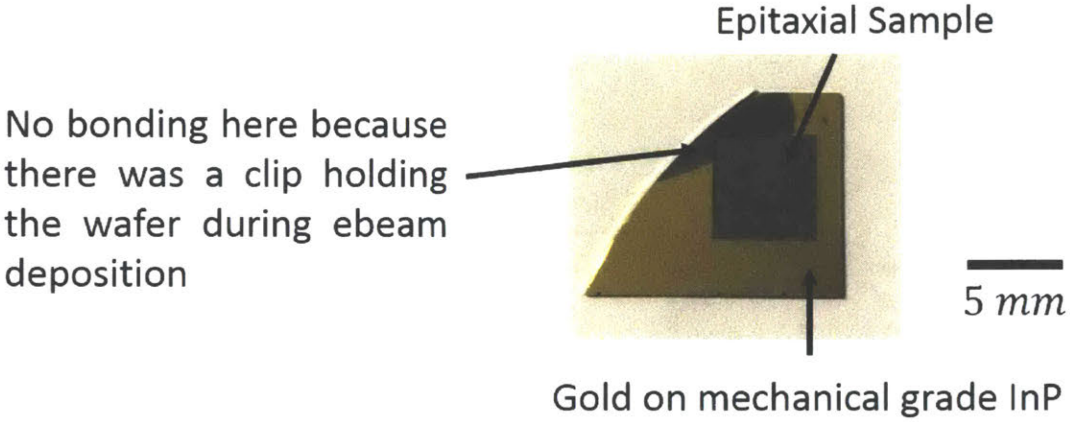

Figure 4-3: A bonded calibration sample. (top view)

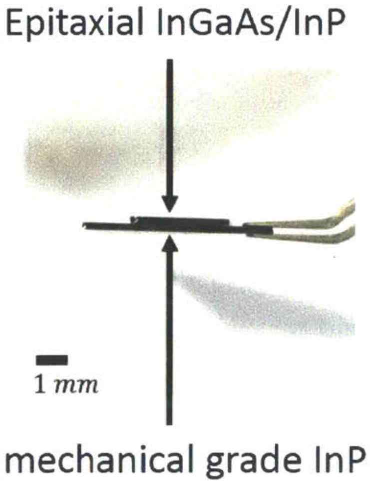

Figure 4-4: A bonded calibration sample. (side view)

The same process then takes place for the two remaining In-P bonds and the In atom and P atom are removed from the crystal as $InCl_3$ and PH_3 (k_2). Here $InCl_3$ is soluble and PH_3 (k_2) is gaseous and they are removed from the system rapidly. [63]

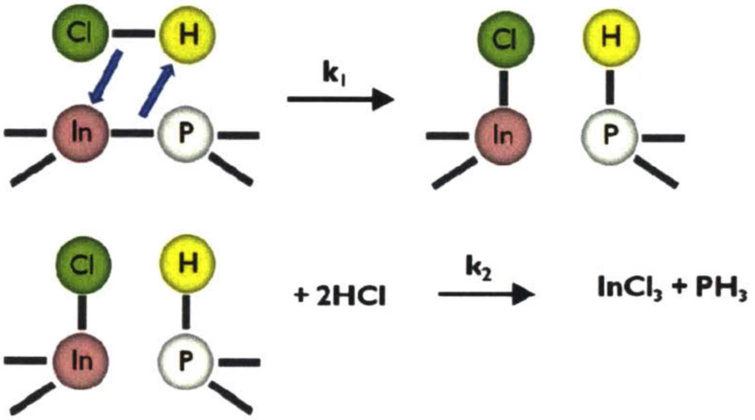

Figure 4-5: Schematic representation of the etching mechanism of InP in HCl solution. [5]

The wet etching of InP in HCl water solution is a relatively fast process. The curve (a) in Fig. 4-6 presents the dependence of the etch rate on the HCl concentration at room temperature. [6] The etch rate is on the order of μm per min. The selectivity between InP and InGaAs is higher than 10^6, which can be considered practically infinite. [61, 62]

In our recipe, the bonded sample is flipped to be n-side up and mounted on glass substrate with crystal bond which protects the sidewall of the sample from the following wet etching. HCl (37% w/w): $H_2O = 3 : 1$ is then used to etch the InP substrate of the epitaxial away and the etch rate is approximately 5 $\mu m/min$. This concentration is indicated in Fig. 4-6 with a red circle and our etch rate is closed to the literature (approximately 3 $\mu m/min$). The etching process lasts for about 1 hour, after which the sample is dismounted from the glass with acetone. A schematic plot of the etching process is present in Fig. 4-7 and a photo of the etched sample is in Fig. 4-8.

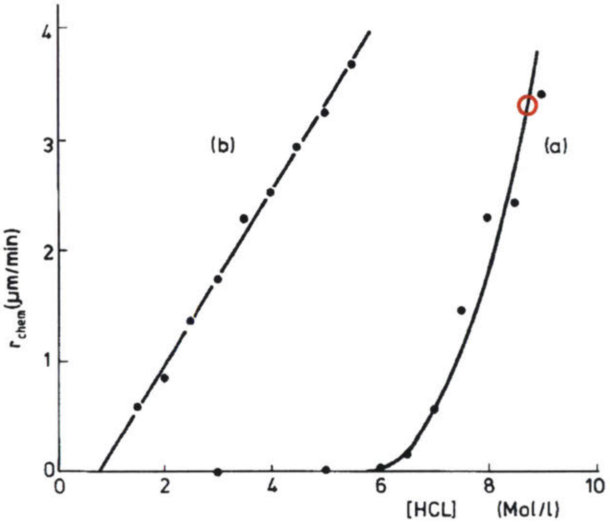

Figure 4-6: The dependence of the etch rate on the HCl concentration in water (a). [6] The red circle indicates the concentration we used in our wet etching.

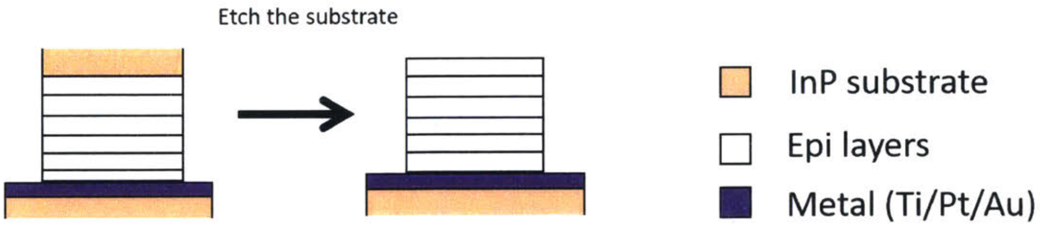

Figure 4-7: A schematic plot of the wet etching processes.

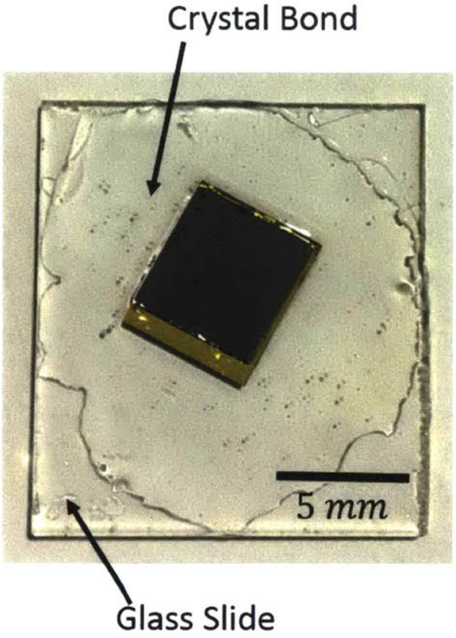

Figure 4-8: A calibration sample after etching with epitaxial layers exposed.

4.2.3 Interference Lithography

We use a STS-CVD machine to deposit a layer of 500 A SiO_2 on the etched sample. The SiO_2 layer serves as hard mask in the reactive ion etching (RIE) step. The selectivity of InP to SiO_2 is higher than 20 : 1. [64]

On the SiO_2, layers of 200 nm XHRI-16 anti-reflective coating (ARC) and 500 nm NR-7 photoresist (PR) are spin-coated. The ARC layer is used here to minimize the reflection at the bottom of the PR layer because the reflection light and the incident light may interfere and this leads to non-uniform dose distribution in the vertical direction. The exposure step is carried out in an interference lithography machine with Lloyd's mirror. The detialed mechanism of Lloyd's mirror can be referred to [65–68]. Here we briefly describe the setup and procedure.

In Fig. 4-9, we present the top view of our Lloyd's mirror. The sample is clipped on a plate and there is a mirror vertical to the plate. The stage below the plate and the mirror can be rotated. The incident light is generated by a 325 nm HeCd laser

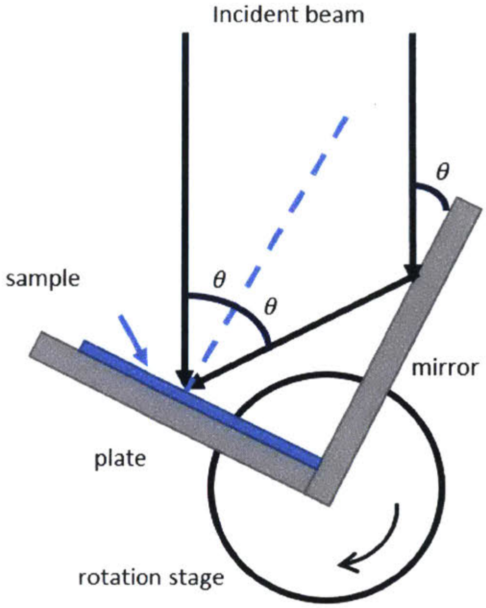

Figure 4-9: A schematic plot of the Lloyd's mirror setup.

and split by the mirror into two coherent beams. One of the beams directly arrives at the sample and the other one is reflected at the mirror before arrival. The two beams interferes with each other on the sample and forms standing wave intensity distribution. The periodicity of the pattern is

$$p = \frac{\lambda}{2\sin\theta} \tag{4.1}$$

where θ is the half angle of the two beams and can be fine tuned by the rotation stage.

In our procedure, after one exposure the sample is rotated 60° and goes through a second exposure. The light intensity distribution is the superposition of the two exposures. In Fig. 4-10 , we present a simulated plot of iso-intensity of the pattern. [7] The total dose is controlled by the time of exposure and requires several calibrations according to the size of the desired holes, or the filling factor. Here the PR we use is negative and thus the less exposed areas will be transferred into holes. Therefore the large dose leads to pattern of small holes.

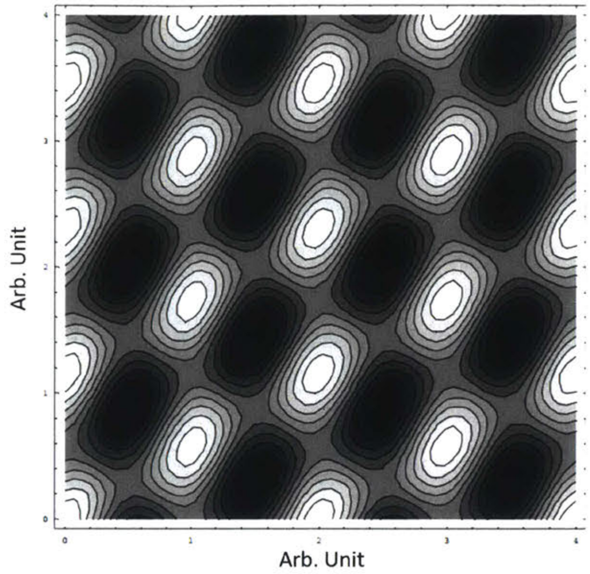

Figure 4-10: Simulated iso-intensity pattern of two-beam interference lithography with 60° rotation. [7]

Elliptical holes, instead of circular ones, are observed in our experiments. This is a natural result of two-beam lithography. (Fig. 4-10) According to our simulations, this degrades the extraction. In Fig. 4-11, we simulate the relative extraction coefficient versus a/b, where a and b are the length of the major and minor axes of the eclipse, respectively. Here $f = 0.5$ is fixed. In our experiment, $a/b \approx 1.35$, which corresponds to approximately 15% loss of the extraction.

In the future, we may modify the setups to solve this problem. One possible method is to use three-beam interference. This method does not require double exposure and can generate circular holes on hexagonal lattice. [69, 70]

After the development, oxygen plasma and fluorine plasma are applied to pattern the ARC and the hard mask, respectively. The residue of the ARC and PR are then removed in an asher machine using oxygen plasma. A schematic plot of the lithography and patterning processes is present in Fig. 4-12.

In Fig. 4-13 we present the A SEM picture of the patterned photoresist and ARC layers. In Fig. 4-14 and Fig. 4-15, the top view and the side view of the patterned hard mask are present. Here we have $p \approx 1.2$ μm and $f \approx 0.3$ based on our previous

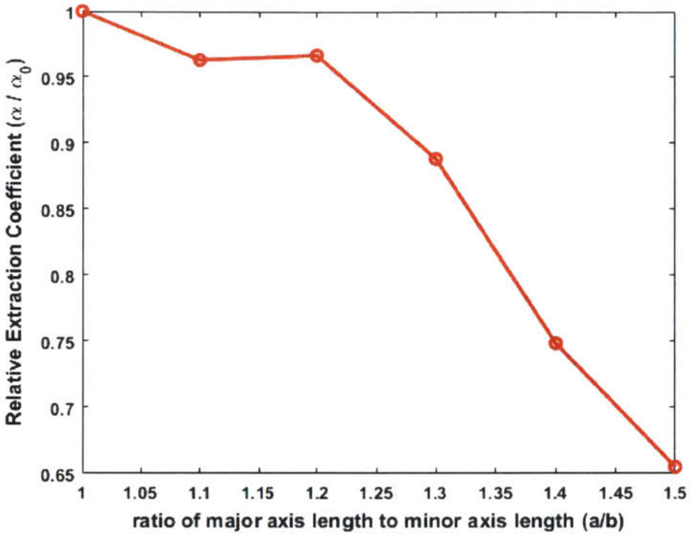

Figure 4-11: Simulated relative extraction coefficient versus a/b

designs. The associated $C_{ex} \approx 65\%$.

4.2.4 Dry Etching of InP

The PhC pattern is etched into the InP in a SAMCO machine where the sample is heated to 220 $°C$. The etching recipe (Recipe 50 in SAMCO at MIT TRL) is based on Cl2/SiCl4/Ar (0.5/3/16 sccm) plasma and the RF power is 40 W. The chamber pressure is 1 Pa during etching. In our experiments, we observed that the etching rate was approximately linear as 6 nm/s.

After the dry etching, the hard mask is removed by HF solution.

A schematic plot of the dry etching process is present in Fig. 4-16. In Fig. 4-17 and Fig. 4-18, the top view and the side view of the patterned InP are present.

4.2.5 Lift-off process for n-contact

At the final step, the sample goes through a lift-off process and the n-contact of grid shape is defined. First, 3 μm of NR9-3000 negative photoresist is spin-coated onto the sample. We then use contact lithography to transfer a grid-shape pattern in the

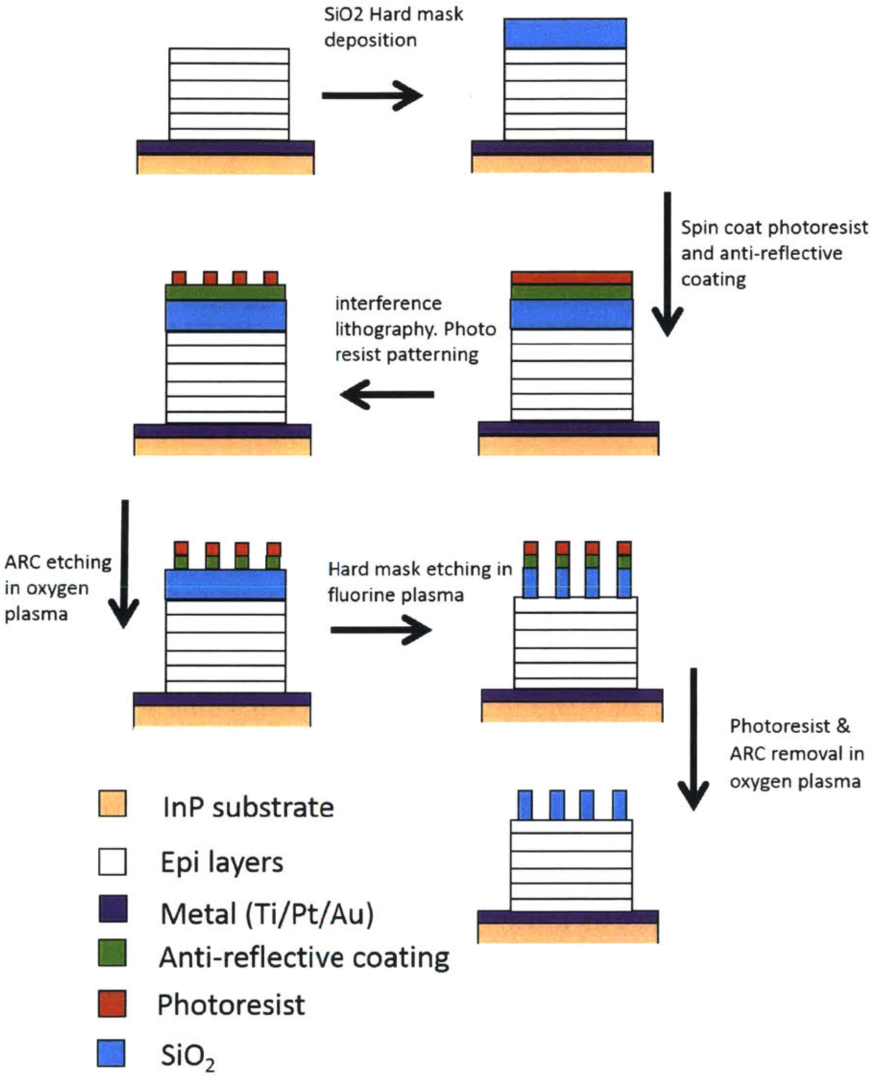

Figure 4-12: A schematic plot of the lithography and patterning processes.

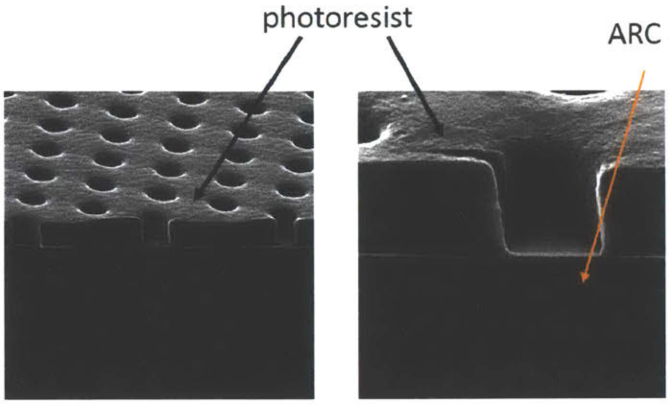

Figure 4-13: A SEM picture of the developed photoresist.

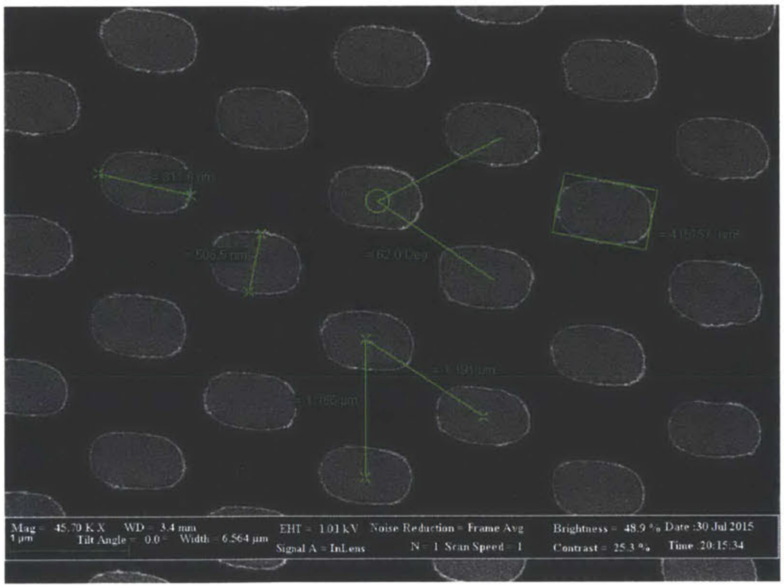

Figure 4-14: A SEM picture of the patterned hard mask (top view).

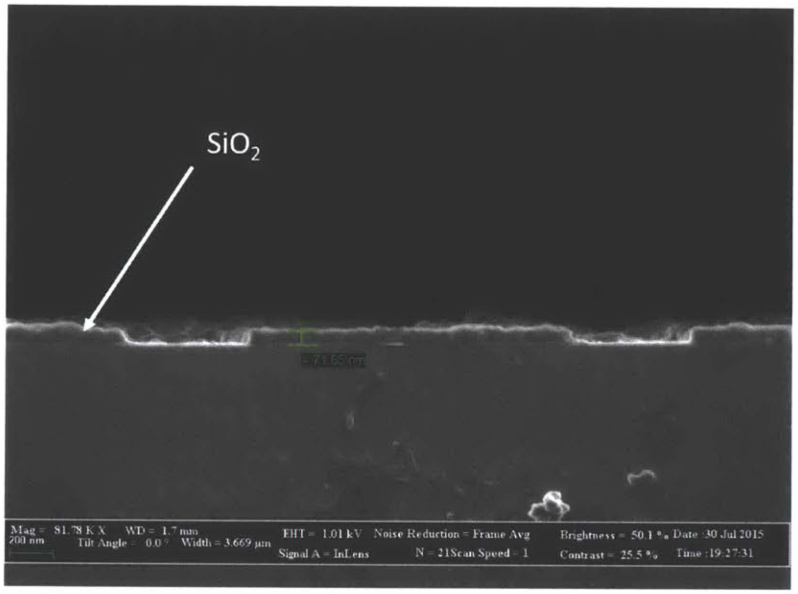

Figure 4-15: A SEM picture of the patterned hard mask (side view). $p \approx 1.2\ \mu m$ and $f \approx 0.3$.

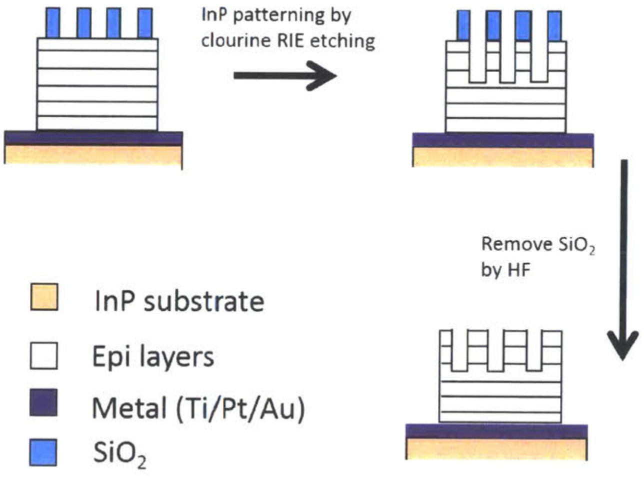

Figure 4-16: A schematic plot of the dry etching processes.

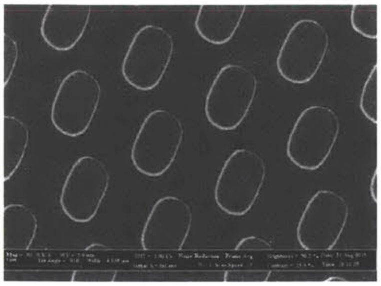

Figure 4-17: A SEM picture of the patterned InP (top view).

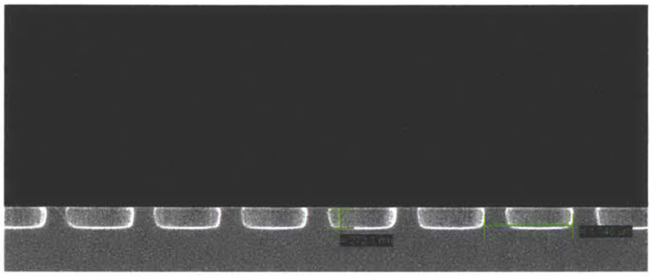

Figure 4-18: A SEM picture of the patterned InP (side view).

photoresist. In Fig. 4-20 we present the design of the contact mask. Girds of various pitches and sizes are designed. Here the photoresist in the exposed area (squares) stays on the sample after development. Ti/Pt/Au of 100/1000/2000 A metal layer is deposited onto the sample using ebeam deposition. Finally, the sample is soaked in acetone for 1 hour to remove the photoresisit and the metal grid is defined. A schematic plot of the dry etching process is present in Fig. 4-19.

The principle of selecting the parameters of the grids is that to minimize the shaded area while to avoid current crowding. In our device, the InGaAs active region is undoped and thus the carrier concentration is on the order of 10^{12} cm^{-3}. [71] The InP layers are approximately doped to 10^{17} cm^{-3}. As a rough estimation, in low bias regime, the ratio of the lateral and vertical resistivity is approximately 10^5. The maximum length of the opening without severe current crowding is $10^5 \times t_{AR} \approx 500$ μm. The width of the gird is kept above 5 μm, which empirically can guarantee a relative clear lift-off pattern. For girds of 500 μm pitch, the shaded area is lower than 2%. However, since no functioning device is obtained, we cannot verify our assumption on current crowding at this time.

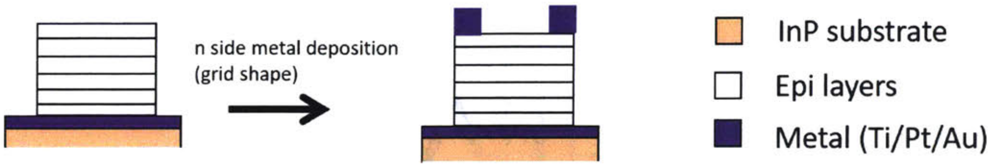

Figure 4-19: A schematic plot of the lift-off process.

In Fig. 4-21, we present the SEM picture of the grid contact.

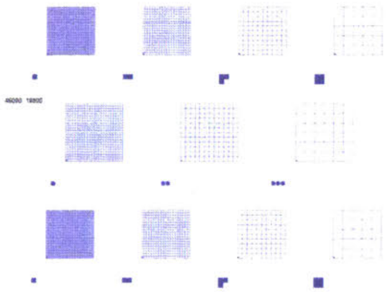

Figure 4-20: Design of the lift-off mask.

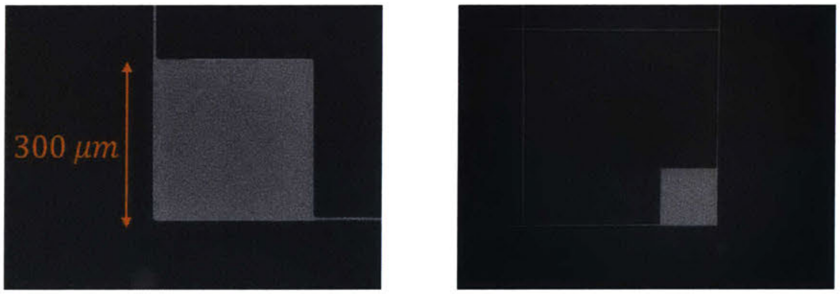

Figure 4-21: SEM pictures of the grid contact.

4.3 Issues on Device samples

The fabrication flow are performed on the device sample but we observe severe issues and no functioning device is obtained. We discuss these issues in this section.

4.3.1 Wet Etching Problem

We observed that the epitaxial layers of bonded samples were all severely broken after wet etching. Ideally, the etching process should stop when the etchant contact the etch stop layer (a 50 nm InGaAs layer in our case). However, the etch stop layer failed to protect the epitaxial layers especially near the edges of the sample, where defects and small holes appeared. As we kept etching the sample in this situation, the defects propagated laterally to the center of the sample and gold underneath was exposed. A photo of a failed sample is present in Fig. 4-22

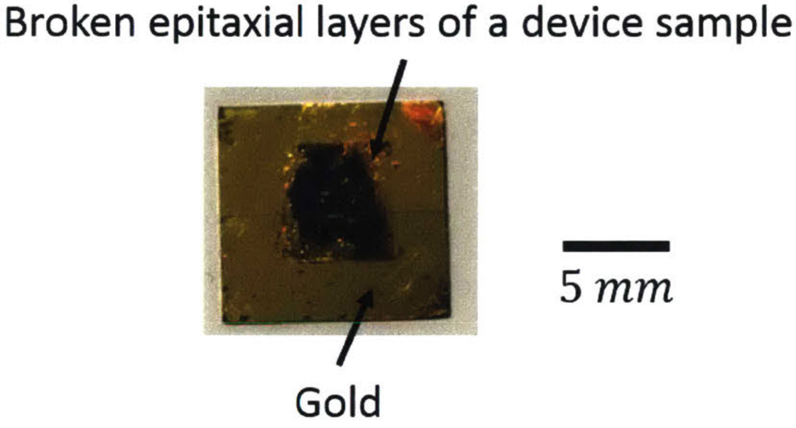

Figure 4-22: A photo of a failed device sample after wet etching.

Based on the phenomenon, we first assumed that the bonding quality was poor only at the edges where the defects appeared. In order to verify this, we used diluted etchant to slow down the etching rate and cover the generated defects in the process. Specifically, once defects appeared, we took the sample from the etchant, covered the edges with crystal bond and then continued the etching. However, we still observed defects appeared at the center of the sample.

Another possible reason is that the etch stop layer is not thick enough since it is only 50 nm for the device sample while it is 300 nm for the calibration sample. In a separate experiment, we skipped the metal-metal bonding process and directly attached the epitaxial layers on a glass slide using crystal bond. These samples, both device and calibration ones, went through the same etching process and the etching quality was equally good. (Fig. 4-23) Hence, the etch stop layer did work for the unbonded samples.

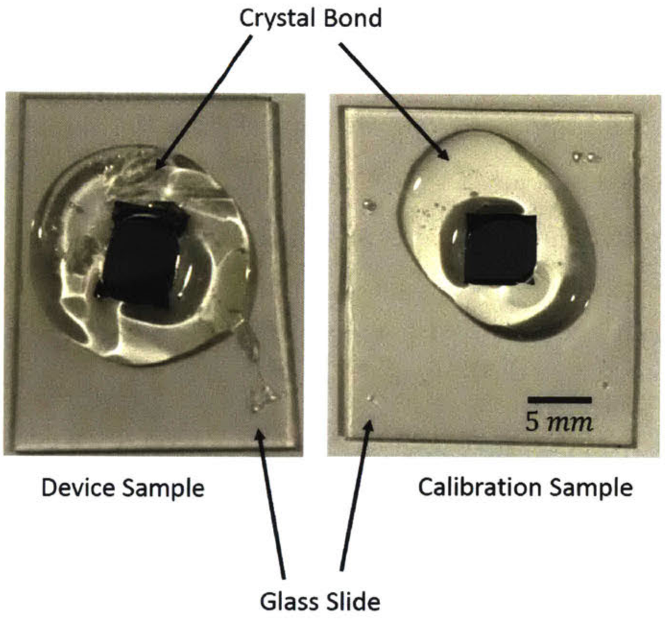

Figure 4-23: Wet etching results of the device and calibration samples without metal-metal bonding.

Therefore, it is highly possible that the wet etching problem was caused by the metal-metal bonding. As is presented in Appendix, the sample temperature goes up to 300 K in approximately 15 min in the process. Since the thermal ramp rate is relatively high, the thermal strain might be non-uniform and lead to cracking of the epitaxial layers. This phenomenon is referred to as thermal shock. [72]

Two facts may contribute to the phenomenon that the device sample is more fragile than the calibration sample given that the InGaAs and InP layers might not be in perfect lattice match. First, the dislocation density and residue stress might be higher in the device samples which have more epitaxial layers and InP/InGaAs interfaces. Second, the epitaxial layers of the device sample are much thinner than those of the calibration sample and thus it is easier for the dislocations to propagate across the layers and lead to layer cracking.

	α (10^{-6} K^{-1})
Pt-Au	15.2
Au	14.2
Ti	8.6
Ta	6.5
InP	4.60
InGaAs	5.66

Table 4.2: The thermal expansion coefficients of some materials.

In the future, we will first perform the bonding and wet etching procedures on InGaAsP/InP device samples which are also provided by our collaborators from Lincoln Lab. The material quality of these samples are higher than the InGaAs/InP ones since our collaborators' specialty lies in the growth and characterization of this particular material system. If it turns out that this material system is easier for us to fabricate, we may consider to switch to InGaAsP/InP LEDs in the future. This requires to re-build of our transport models based on the different material properties. We will also try to lower the thermal ramp rate during the bonding process. This should effectively lower the thermal expansion rates of the materials and reduce non-uniformity of the strain field.

It might also be helpful as we will change the metal contact to Ta/Au. As we discussed in the previous chapter, Ta/Au contact is chosen due to optical considerations. It turns out that Ta is also better for bonding. We list the thermal expansion coefficients (α) of some related materials in Tab. 4.2. The difference in thermal expansion coefficient of Ta and InP/InGaAs is smaller than Ti and InP/InGaAs. (Tab. 4.2) Therefore, as we switch to the Ta/Au contact, the bonding and etching should yield better results.

4.3.2 Micromasking Effect

We have performed the lithography and dry etching on the bonded samples which had relatively good quality after wet etching. Unfortunately, the etched pattern was not satisfying, and specifically, micromaksing effect, or 'grass effect', was observed under SEM. (Fig. 4-24)

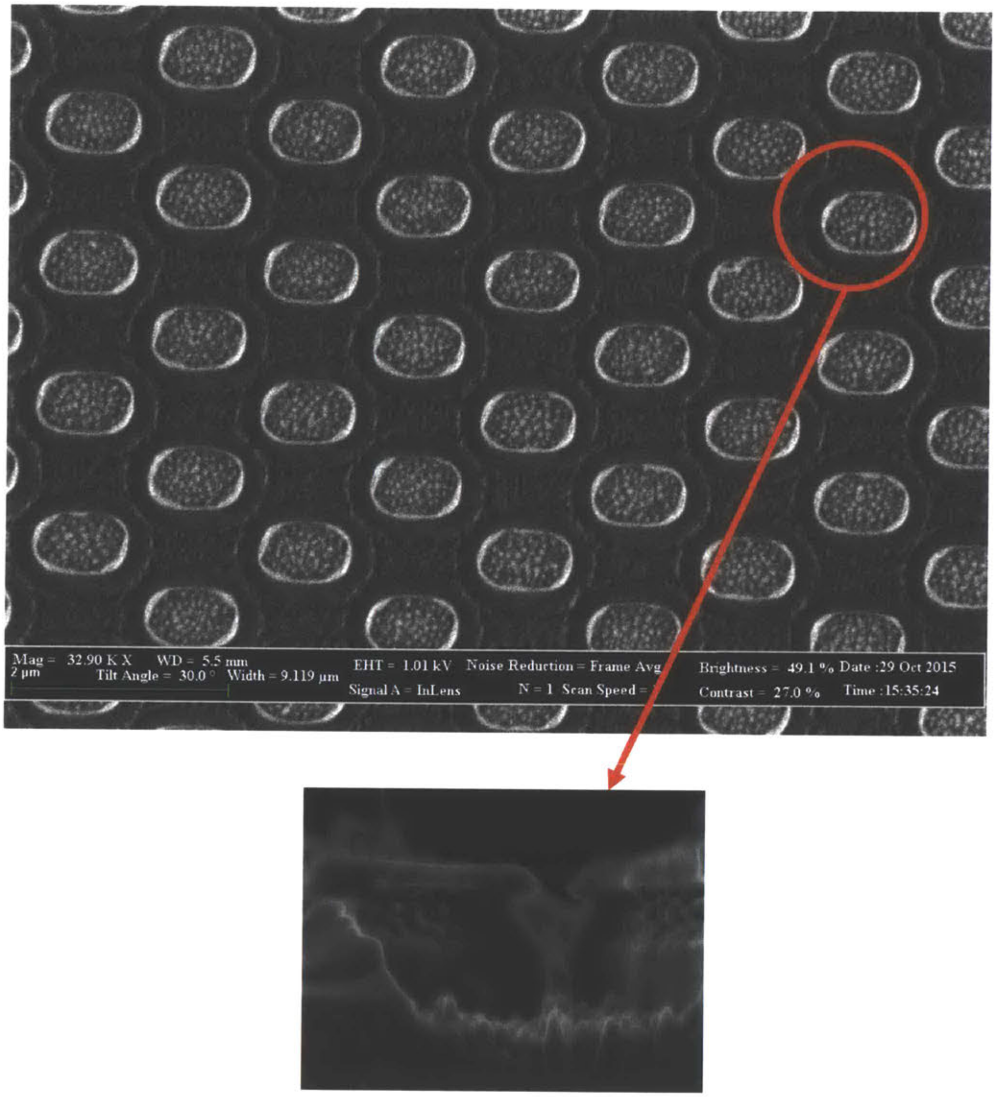

Figure 4-24: A SEM photo of the micromasking effect. Here the metal contact of the sample is Ti/Au.

It is well known that gold contamination causes the mircromasking effect. [73, 74] In our case, there are two possible sources of gold contamination. One is that gold may diffuse through the sample during the bonding process. However, this is unlikely to happen with standard Ti/Pt/Au contact which includes the Pt diffusion blocking layer. The other possible source is that gold particles might be sputtered onto the sample during the dry etching. This is likely the reason because defects are generated during the wet etching and thus gold can be exposed to the plasma. Therefore, if we solve the wet etching problem, the micromasking effect should also be fixed.

4.4 Conclusion

In this chapter, we review the fabrication recipe we developed. Each step was performed on calibration samples and the associated result was satisfying. However, we observed severe wet etching problem and micromasking effect for our device samples. It is highly possible that the InP/InGaAs samples have relatively high lattice mismatch and the metal-metal bonding process causes the failure. In the future, we will test the procedures on InGaAsP/InP samples which tend to have better material quality. We will also lower the thermal ramp rate during bonding to eliminate the possible thermal shock.

Chapter 5

Conclusion and Future Work

In this chapter, we will first summarize our research on simulation, design and fabrication of PhC LEDs for electroluminescent cooling. After that, we will state possible future work including improvement of modeling and modification of the fabrication process.

5.1 Conclusion

The goal of our work is to design and fabricate LEDs which exhibit temperature drop due to electroluminescent cooling. In this thesis, our work can be divided into three parts. We firstly optimized the PhC structure on our LED to maximize the extraction coefficient. Based on the PhC design, transport and thermal models were investigated. Finally, we developed and tested a fabrication process for this design.

5.1.1 Optical Modeling

We first point out that the ELC effect is easily overwhelmed by the ambient heat flux since the cooling power is only on the order of mW/cm^2. In order to detect a temperature drop of mK, we have to eliminate the package and extraction structures that are commonly used in commercial encapsulated LEDs because they tend to bring large surface area and thermal mass. As for extraction structures of unencapsulated LEDs, we select PhC rather than textured surfaces because the former is more straightforward to model and the performance is thus more predictable.

In the first chapter, we optimized our PhC structure to maximize the extraction coefficient α_{ext}. The model was built in OmniSim 4.0, which is a 3D-FDTD engine. We benchmarked our model with Fan *et al.*'s work [39] and obtained similar extraction results. We consider four parameters which are the hole depth d, the unetched core thickness t, the pitch of the patter p, and the filling factor f. Each of these parameters has profound effects on the extraction. Due to the restriction of computational resources, we separated these parameters into three groups and optimize the structure over each group. The best structure we obtained has $\alpha_{ext} \approx 1.5 \times 10^3\ cm^{-1}$ with $t = 0.27\ \mu m$, $d = 0.39\ \mu m$, $p = 0.74\ \mu m$ and $f = 0.5$. Besides the FDTD simulations, the dependence on parameters are also verified by several simple physical models.

Our extraction coefficient corresponds to an extraction length of approximately 6 μm. This is close to the extraction length ($\approx\ 4\mu m$) in Fan *et al.*'s work. [39] However, it is worthwhile to point out that unlike a lossless model, our model also includes metal loss and other absorption as competing processes against extraction. Therefore, we define our extraction efficiency based on the extraction and absorption coefficients instead of the ratio of extracted and trapped power.

5.1.2 Transport and Thermal Modeling

In Chapter 2, we built transport and thermal models to simulate the performance of the device. The transport model is based on SimWindows, which solves the drift-diffusion equations and the recombination rate equations. In the model, we have taken metal loss and band edge absorption into account. The active region thickness t_{AR}, which is associated with the band edge absorption, is optimized here. We obtained $t_{AR} \approx 5\ nm$ as the optimum result. The maximum cooling power generated by this device is approximately 300 $\mu W/cm^2$ and the extraction efficiency C_{ex} is approximately 76%.

The thermal models are solvers of Fourier equations in air and vacuum. In air, the heat flux from the ambient is considered and the maximum temperature drop is approximately 0.1 K. In vacuum, the Joule heating and the heat flux from the wires are the main sources of heating. The maximum temperature drop is approximately 0.5 K.

5.1.3 Fabrication

In Chapter 3, we reviewed the fabrication process which we developed for the designed LEDs and presented the preliminary results. The fabrication process has three main steps including metal-metal thermal bonding, wet etching of InP substrate, and interference lithography for PhC patterning. Each step is performed on a calibration sample and all yield relatively satisfying outcomes. However, device samples, which have more complicated epitaxial structure, are severely broken after wet etching. Evidence show that this might be caused by layer cracking which formed during the thermal bonding step. Further investigations on this issue have to be carried out.

5.2 Future Work

In this section, we will describe how to improve our models to fix some flaws. We also summarize the future work in order to solve the wet etching problem.

5.2.1 Modeling Improvement

There are two flaws in our models. First, in the FDTD simulations, we only consider the in-plane polarization of the emitting dipole source. Although this is close to the cases of C-HH transition in ideal quantum wells, it is desired to also consider the vertical polarization for active regions with finite thickness and C-LH transition. Our simulation shows that the extraction efficiency is lower than 50% for the vertical polarization in our current design. The poor performance is partly due to the fact that we specifically designed our extraction structure for in-plane polarization. In the future, we will simulate the extraction based on the ratio of different polarization. If the component of the vertical polarization is relatively high and that the overall extraction efficiency is not enough for cooling, we have to re-design the optical structure. For example, if 20% of the emitting source is vertically polarized, we have $C_{ex} \approx 70\%$ and the cooling power is approximately 15 $\mu W/cm^2$. Here the temperature drop is approximately 5 mK and might be hard to be detected by thermocouples.

The other issue, which might be more important, that needs further investigation is the simulations of the loss processes. As mentioned above, the extraction process is simulated in a 3D-FDTD engine and is 'modeless', while the loss processes are analyzed only for the fundamental mode. Although the fundamental mode usually carries most of the optical energy, the separation of the two kinds of simulations make our models inconsistent to some extent. In the future, we will use more sophisticated software, such as CST MICROWAVE STUDIO which simulates the extraction and loss processes simultaneously. Our current results can serve as meaningful references.

5.2.2 Fabrication Process Modification

As we mentioned the Chapter 4, the dislocation density of the device samples might be high due to the lattice mismatch of InGaAs and InP. We can test this hypothesis by performing the same bonding and wet etching procedures on InGaAsP/InP samples which tend to have low dislocation density. The InGaAsP/InP samples have already been provided by our collaborators, whose specialty lies in the growth and characterization of this particular material system. If it turns out that this material system is easier for our fabrication, we may consider switch to InGaAsP/InP LEDs in the future. This requires to re-build of our transport models based on different materials properties.

As for the InGaAs samples, we will lower the thermal ramp rate during bonding because this reduces the local temperature gradient and may help eliminate the layer cracking. In the EV501 machine, there is no direct setting of ramp rate and the only parameter of heating is the desired temperature. However, we can effectively achieve a lower ramp rate by setting multiple desired temperatures sequentially.

5.3 Summary

Conclusively, the novelties of our design include

- We optimized our LED at $qV \approx 0.5\hbar\omega$ while the existing ultra-efficient LEDs operate at $qV < kT$. [14,27] We therefore expect over 10^6 higher cooling power than earlier design.
- We proposed a novel unencapsulated structure with a PhC grating and a back reflector which significantly lower the thermal mass and surface area while remain a reasonably high extraction efficiency ($\approx 76\%$). This makes the observation of ELC temperature drop of 100 mK possible in ambient.
- Our model is relatively complete. We considered multiple physical processes in our device. The competing processes against extraction including metal loss and active region absorption were taken into account. Based on this model, various parameters, such as the active region thickness and doping level, are co-optimized.

Appendix A

Fabrication Flow

Wafer bonding

Step	Lab	Machine	Comments
Wafer cleaving	TRL		Cleave MBE wafer into pieces 1 cm x 1 cm or 2 cm x 2cm
Deposit surface metal	TRL	e-beam-Au	Deposit Zn/Au 150/2000 A on MBE grown wafer. Deposit Zn/Au 150/2000 A on bare InP wafer front side.
(Optional) Deposit surface metal	TRL	AJA-TRL	Deposit Ti/Au 150/2000 A on MBE grown wafer. Deposit Ti/Au 150/2000 A on bare InP wafer frontside.
Surface clean	TRL		Blow dry and inspect under u-scope
Bonding	TRL	EV501	Replace quartz pressure plate with steel plate Use 4" bonder chuck (Au). Align dies on chuck by hand Place 4" steel electrode (no bow) on top of wafer stack w/ graphite spacers Bond dies in bonder – 300-400 C – 60 min – pressure ~ 4MPa – vacuum (EV501 recipe: zhli/bonding_new.aba)
(Optional) Anneal	TRL	EV501	Anneal for 45min at 300C, in N2 ambient (EV501 recipe: zhli/bonding_new.aba)

Wet etching

Step	Lab	Machine	Comments
Mount on glass substrate with Crystal bond	TRL		Protect sidewalls
Wet etching	TRL	Acid hood	HCl: H_2O = 3: 1 (selectivity: practically infinite) Etch rate ~ 5 um/min ~1 hour Plastic beaker.
Wet etching	TRL	Acid hood	H_2SO_4: H_2O_2: H_2O= 1: 1: 2 2 um/min (Selectivity: high?) ~3s Glass beaker.
Dismount	TRL		Heat, three solvent clean, ultrasonic clean

SiO_2 deposition, Interference Lithography and hard mask patterning

Step	Lab	Machine	Comments
SiO_2 deposition	TRL	STS-CVD	Deposit 500A SIO2 on front bonded samples
Deposit Anti-reflective coating	NSL	Spin coater	XHRI-16 (~200 nm) 2.2 k rpms (60s) Bake at 190 C for 60 s
Photoresist coating	NSL	Spin coater	0.5 um negative photoresist NR-7; 0.8k rpms (60s) Baking 150°C for 60 s.

Photoresist exposure	NSL	Lloyd's mirror	Coherent beams. Double exposure. Lloyd's mirror. HeCd laser. (325 nm) with 0.22 uW/cm2. Exposure time ~ 45 s (The dose depends on the tilting angle)
Development	NSL		Prebake 100 C, 60s. Developer, RD6: DI water = 3: 1. Develop time ~ 60 sec. Rinse in DI water and dry with nitrogen.

Chlorine Etch for InP

Step	Lab	Machine	Comments
Remove ARC and photoresist	TRL	Asher-TRL	Ash for 45 min. (Or 5 min in NSL.)
InP substrate dry etch	TRL	SAMCO	Run standard Cl clean, then precondition chamber using InP dummies for 10 min using recipe 50 (ICP120W, RF 40W, 0.5/3/16 sccm Cl2/SiCl4/Ar, 1 Pa) Etch samples using recipe # 50 for 50 s. SiO2 as mask.
Hard mask removal (wet etch)	TRL	Acid hood	BOE. 700A / min. 3 min.

N-side metal deposition and lift-off (NSL)

Step	Lab	Machine	Comments
Photoresist coating	NSL	Spin coater	3 um negative NR9-3000 3k rpms (60s) Bake at 150 C (60s)
Photoresist exposure	NSL	TAMARACK	UV board band light source. 4 min.@ 2.2mJ/cm2
Development	NSL		Prebake 100 C, 60s. Developer RD6, 30s Rinse in DI water and dry with nitrogen.
Evaporation	TRL	e-beam-Au	Deposit Ti/Au 150/2000 A.
Evaporation (optional)	NSL		Leave Jim a message. 'deposit Ti/Au 150/2000 A.'
Lift off	NSL		Acetone. ~60 min. Face down.

Wire bonding

Step	Lab	Machine	Comments
Wire bonding	ICL	goldwire	

Bibliography

[1] L. A. Coldren, S. W. Corzine, and M. L. Mashanovitch, *Diode lasers and photonic integrated circuits*, vol. 218. John Wiley & Sons, 2012.

[2] R. Newman, "Optical properties of n-type inp," *Physical Review*, vol. 111, no. 6, p. 1518, 1958.

[3] H. C. Casey and P. L. Carter, "Variation of intervalence band absorption with hole concentration in ptype inp," *Applied Physics Letters*, vol. 44, no. 1, pp. 82–83, 1984.

[4] S. Adachi, *Physical properties of III-V semiconductor compounds.* John Wiley & Sons, 1992.

[5] D. Cuypers, S. De Gendt, S. Arnauts, K. Paulussen, and D. van Dorp, "Wet chemical etching of inp for cleaning applications i. an oxide formation/oxide dissolution model," *ECS Journal of Solid State Science and Technology*, vol. 2, no. 4, pp. P185–P189, 2013.

[6] P. Notten, "The etching of inp in hcl solutions: a chemical mechanism," *Journal of The Electrochemical Society*, vol. 131, no. 11, pp. 2641–2644, 1984.

[7] F. Quiñónez, J. Menezes, L. Cescato, V. Rodriguez-Esquerre, H. Hernandez-Figueroa, and R. Mansano, "Band gap of hexagonal 2d photonic crystals with elliptical holes recorded by interference lithography," *Optics express*, vol. 14, no. 11, pp. 4873–4879, 2006.

[8] E. F. Schubert, T. Gessmann, and J. K. Kim, *Light emitting diodes.* Wiley Online Library, 2005.

[9] S. Farrens, "Latest metal technologies for 3d integration and mems wafer level bonding," 2008.

[10] P. Pringsheim, "Zwei bemerkungen über den unterschied von lumineszenz- und temperaturstrahlung," *Zeitschrift für Physik*, vol. 57, no. 11, pp. 739–746, 1929.

[11] R. I. Epstein, M. I. Buchwald, B. C. Edwards, T. R. Gosnell, C. E. Mungan, *et al.*, "Observation of laser-induced fluorescent cooling of a solid," *Nature*, vol. 377, no. 6549, pp. 500–503, 1995.

[12] D. V. Seletskiy, S. D. Melgaard, S. Bigotta, A. Di Lieto, M. Tonelli, and M. Sheik-Bahae, "Laser cooling of solids to cryogenic temperatures," *Nature Photonics*, vol. 4, no. 3, pp. 161–164, 2010.

[13] J. Zhang, D. Li, R. Chen, and Q. Xiong, "Laser cooling of a semiconductor by 40 kelvin," *Nature*, vol. 493, no. 7433, pp. 504–508, 2013.

[14] P. Santhanam, D. J. Gray, and R. J. Ram, "Thermoelectrically pumped light-emitting diodes operating above unity efficiency," *Physical Review Letters*, vol. 108, no. 9, p. 097403, 2012. PRL.

[15] J. Oksanen and J. Tulkki, "Thermophotonic heat pumpa theoretical model and numerical simulations," *Journal of applied physics*, vol. 107, no. 9, p. 093106, 2010.

[16] O. Heikkila, J. Oksanen, and J. Tulkki, "Ultimate limit and temperature dependency of light-emitting diode efficiency," *Journal of Applied Physics*, vol. 105, no. 9, p. 093119, 2009.

[17] J. Tauc, "The share of thermal energy taken from the surroundings in the electro-luminescent energy radiated from ap-n junction," *Cechoslovackij fiziceskij zurnal*, vol. 7, no. 3, pp. 275–276, 1957.

[18] M. A. Weinstein, "Thermodynamic limitation on the conversion of heat into light," *Journal of the Optical Society of America*, vol. 50, no. 6, pp. 597–602, 1960.

[19] P. T. Landsberg and D. A. Evans, "Thermodynamic limits for some light-producing devices," *Physical Review*, vol. 166, no. 2, pp. 242–246, 1968. PR.

[20] P. T. Landsberg and G. Tonge, "Thermodynamic energy conversion efficiencies," *Journal of Applied Physics*, vol. 51, no. 7, pp. R1–R20, 1980.

[21] W. Nakwaski, "Optical refrigeration in light-emitting diodes," *Electronic Technology*, vol. 13, p. 61, 1982.

[22] S.-Q. Yu, J.-B. Wang, D. Ding, S. Johnson, D. Vasileska, and Y.-H. Zhang, "Fundamental mechanisms of electroluminescence refrigeration in heterostructure light-emitting diodes," *Proc. SPIE Int. Soc. Opt. Eng.*, vol. 6486, pp. 648604–648604-6, 2007.

[23] K. Lehovec, C. A. Accardo, and E. Jamgochian, "Light emission produced by current injected into a green silicon-carbide crystal," *Physical Review*, vol. 89, no. 1, pp. 20–25, 1953. PR.

[24] G. C. Dousmanis, C. W. Mueller, H. Nelson, and K. G. Petzinger, "Evidence of refrigerating action by means of photon emission in semiconductor diodes," *Physical Review*, vol. 133, no. 1A, pp. A316–A318, 1964. PR.

[25] J. Xue, Y. Zhao, S.-H. Oh, W. F. Herrington, J. S. Speck, S. P. DenBaars, S. Nakamura, and R. J. Ram, "Thermally enhanced blue light-emitting diode," *Applied Physics Letters*, vol. 107, no. 12, p. 121109, 2015.

[26] C. A. Hurni, A. David, M. J. Cich, R. I. Aldaz, B. Ellis, K. Huang, A. Tyagi, R. A. DeLille, M. D. Craven, F. M. Steranka, and M. R. Krames, "Bulk gan flip-chip violet light-emitting diodes with optimized efficiency for high-power operation," *Applied Physics Letters*, vol. 106, no. 3, p. 031101, 2015.

[27] P. Santhanam, D. Huang, R. J. Ram, M. A. Remennyi, and B. A. Matveev, "Room temperature thermo-electric pumping in mid-infrared light-emitting diodes," *Applied Physics Letters*, vol. 103, no. 18, p. 183513, 2013.

[28] D. J. Gray, P. Santhanam, and R. J. Ram, "Design for enhanced thermo-electric pumping in light emitting diodes," *Applied Physics Letters*, vol. 103, no. 12, p. 123503, 2013.

[29] R. J. Osczevski, "The basis of wind chill," *Arctic*, vol. 48, no. 4, pp. 372–382, 1995.

[30] D. Garbuzov, "Reradiation effects, lifetimes and probabilities of band-to-band transitions in direct a3b5 compounds of gaas type," *Journal of Luminescence*, vol. 27, no. 1, pp. 109–112, 1982.

[31] R. Windisch, C. Rooman, S. Meinlschmidt, P. Kiesel, D. Zipperer, G. H. Dhler, B. Dutta, M. Kuijk, G. Borghs, and P. Heremans, "Impact of texture-enhanced transmission on high-efficiency surface-textured light-emitting diodes," *Applied Physics Letters*, vol. 79, no. 15, pp. 2315–2317, 2001.

[32] C. Rooman, M. Kuijk, S. D. Jonge, and P. Heremans, "High-efficiency algainp thin-film leds using surface-texturing and waferbonding with conductive epoxy," *IEEE Photonics Technology Letters*, vol. 17, no. 12, pp. 2649–2651, 2005.

[33] I. Schnitzer, E. Yablonovitch, C. Caneau, T. Gmitter, and A. Scherer, "30external quantum efficiency from surface textured, thinfilm lightemitting diodes," *Applied Physics Letters*, vol. 63, no. 16, pp. 2174–2176, 1993.

[34] V. Haerle, B. Hahn, S. Kaiser, A. Weimar, S. Bader, F. Eberhard, A. Plssl, and D. Eisert, "High brightness leds for general lighting applications using the new thingan-technology," *Physica Status Solidi A Applications and Material Science*, vol. 201, no. 12, pp. 2736–2739, 2004.

[35] J. J. Wierer, D. A. Steigerwald, M. R. Krames, J. J. OShea, M. J. Ludowise, G. Christenson, Y.-C. Shen, C. Lowery, P. S. Martin, S. Subramanya, W. Gtz, N. F. Gardner, R. S. Kern, and S. A. Stockman, "High-power algainn flip-chip light-emitting diodes," *Applied Physics Letters*, vol. 78, no. 22, pp. 3379–3381, 2001.

[36] M. J. Cich, R. I. Aldaz, A. Chakraborty, A. David, M. J. Grundmann, A. Tyagi, M. Zhang, F. M. Steranka, and M. R. Krames, "Bulk gan based violet light-emitting diodes with high efficiency at very high current density," *Applied Physics Letters*, vol. 101, no. 22, p. 223509, 2012.

[37] A. David, H. Benisty, and C. Weisbuch, "Optimization of light-diffracting photonic-crystals for high extraction efficiency leds," *Journal of Display Technology*, vol. 3, no. 2, pp. 133–148, 2007.

[38] C. Wiesmann, K. Bergenek, N. Linder, and U. T. Schwarz, "Photonic crystal leds designing light extraction," *Laser and Photonics Reviews*, vol. 3, no. 3, pp. 262–286, 2009.

[39] S. Fan, P. R. Villeneuve, J. D. Joannopoulos, and E. F. Schubert, "High extraction efficiency of spontaneous emission from slabs of photonic crystals," *Physical Review Letters*, vol. 78, no. 17, pp. 3294–3297, 1997. PRL.

[40] A. A. Erchak, D. J. Ripin, S. Fan, P. Rakich, J. D. Joannopoulos, E. P. Ippen, G. S. Petrich, and L. A. Kolodziejski, "Enhanced coupling to vertical radiation using a two-dimensional photonic crystal in a semiconductor light-emitting diode," *Applied Physics Letters*, vol. 78, no. 5, pp. 563–565, 2001.

[41] J. J. Wierer, A. David, and M. M. Megens, "Iii-nitride photonic-crystal light-emitting diodes with high extraction efficiency," *Nature Photonics*, vol. 3, no. 3, pp. 163–169, 2009. 10.1038/nphoton.2009.21.

[42] A. David, "Surface-roughened light-emitting diodes: An accurate model," *Journal of Display Technology*, vol. 9, no. 5, pp. 301–316, 2013.

[43] E. F. Schubert, N. E. J. Hunt, R. J. Malik, M. Micovic, and D. L. Miller, "Temperature and modulation characteristics of resonant-cavity light-emitting diodes," *Journal of Lightwave Technology*, vol. 14, pp. 1721–1729, Jul 1996.

[44] E. F. Schubert, Y. Wang, A. Y. Cho, L. Tu, and G. J. Zydzik, "Resonant cavity lightemitting diode," *Applied Physics Letters*, vol. 60, no. 8, 1992.

[45] W. Streifer, D. Scifres, and R. Burnham, "Analysis of grating-coupled radiation in gaas:gaalas lasers and waveguides - i," *IEEE journal of quantum electronics*, vol. 12, no. 7, pp. 422–428, 1976.

[46] G. Taylor and C. Kwan, "Determination of diffraction efficiency for a second-order corrugated waveguide," *IEEE journal of quantum electronics*, vol. 33, no. 2, pp. 176–186, 1997.

[47] A. Haug, "Free-carrier absorption in semiconductor lasers," *Semiconductor Science and Technology*, vol. 7, no. 3, p. 373, 1992.

[48] F. Stern and J. M. Woodall, "Photon recycling in semiconductor lasers," *Journal of Applied Physics*, vol. 45, no. 9, 1974.

[49] H. Benisty, H. D. Neve, and C. Weisbuch, "Impact of planar microcavity effects on light extraction-part ii: selected exact simulations and role of photon recycling," *IEEE Journal of Quantum Electronics*, vol. 34, pp. 1632–1643, Sep 1998.

[50] A. Marti, J. L. Balenzategui, and R. F. Reyna, "Photon recycling and shockleys diode equation," *Journal of Applied Physics*, vol. 82, no. 8, 1997.

[51] E. Garmire and H. Stoll, "Propagation losses in metal-film-substrate optical waveguides," *IEEE journal of quantum electronics*, vol. 8, no. 10, pp. 763–766, 1972.

[52] M. N. Polyanskiy, "Refractive index database. http://refractiveindex.info," 2016.

[53] D. W. Winston, *Physical simulation of optoelectronic semiconductor devices.* PhD thesis, 1996.

[54] T. H. Gfroerer, E. A. Cornell, and M. W. Wanlass, "Efficient directional spontaneous emission from an ingaas/inp heterostructure with an integral parabolic reflector," *Journal of Applied Physics*, vol. 84, no. 9, pp. 5360–5362, 1998.

[55] S. Farrens, "Metal based wafer bonding techniques for wafer level packaging," *Süss Report*, pp. 14–7, 2010.

[56] E. Jung, A. Ostmann, M. Wiemer, I. Kolesnik, and M. Hutter, "Soldered sealing process to assemble a protective cap for a mems csp," in *Design, Test, Integration and Packaging of MEMS/MOEMS 2003. Symposium on*, pp. 255–260, IEEE, 2003.

[57] T. Shimatsu and M. Uomoto, "Atomic diffusion bonding of wafers with thin nanocrystalline metal films," *Journal of Vacuum Science & Technology B*, vol. 28, no. 4, pp. 706–714, 2010.

[58] S. Farrens, "Wafer-bonding technologies and strategies for 3d ics," in *Wafer Level 3-D ICs Process Technology*, pp. 1–35, Springer, 2008.

[59] C. H. Tsau, S. M. Spearing, and M. A. Schmidt, "Characterization of wafer-level thermocompression bonds," *Journal of Microelectromechanical Systems*, vol. 13, no. 6, pp. 963–971, 2004.

[60] E. Kuphal, "Low resistance ohmic contacts to n-and p-inp," *Solid-State Electronics*, vol. 24, no. 1, pp. 69–78, 1981.

[61] K. Hjort, "Sacrificial etching of iii-v compounds for micromechanical devices," *Journal of Micromechanics and Microengineering*, vol. 6, no. 4, p. 370, 1996.

[62] C. Seassal, J. Leclercq, and P. Viktorovitch, "Fabrication of inp-based freestanding microstructures by selective surface micromachining," *Journal of micromechanics and microengineering*, vol. 6, no. 2, p. 261, 1996.

[63] P. H. Notten, J. E. Meerakker, and J. J. Kelly, *Etching of III-V Semiconductors: An Electrochemical Approach.* Elsevier Science Ltd, 1991.

[64] B. Docter, E. Geluk, M. Sander-Jochem, F. Karouta, and M. Smit, "Deep etching of dbr gratings in inp using cl2 based icp processes," in *Proc. Symp. IEEE/LEOS Benelux Chapter (Eindhoven, the Netherlands)*, Citeseer, 2006.

[65] L. Suslik, D. Pudis, J. Skriniarova, I. Martincek, I. Kubicova, and J. Kovac, "2d photonic structures for optoelectronic devices prepared by interference lithography," *Physics Procedia*, vol. 32, pp. 807–813, 2012.

[66] J. de Boor, N. Geyer, U. Gsele, and V. Schmidt, "Three-beam interference lithography: upgrading a lloyd's interferometer for single-exposure hexagonal patterning," *Optics letters*, vol. 34, no. 12, pp. 1783–1785, 2009.

[67] L. Chen and A. V. Nurmikko, "Fabrication and performance of efficient blue light emitting iii-nitride photonic crystals," *Applied physics letters*, vol. 85, no. 17, pp. 3663–3665, 2004.

[68] A. Chincholi, S. Banerjee, J.-S. Huang, and D. Klotzkin, "Parallel fabrication of photonic crystals (pc) using interference lithography for integrated waveguide-pc devices," in *Adaptive Optics: Methods, Analysis and Applications*, p. JWB10, Optical Society of America.

[69] J. de Boor, N. Geyer, U. Gösele, and V. Schmidt, "Three-beam interference lithography: upgrading a lloyd's interferometer for single-exposure hexagonal patterning," *Optics letters*, vol. 34, no. 12, pp. 1783–1785, 2009.

[70] J. L. Stay, G. M. Burrow, and T. K. Gaylord, "Three-beam interference lithography methodology," *Review of Scientific Instruments*, vol. 82, no. 2, p. 023115, 2011.

[71] S. Paul, J. Roy, and P. Basu, "Empirical expressions for the alloy composition and temperature dependence of the band gap and intrinsic carrier density in gaxin1- xas," *Journal of applied physics*, vol. 69, no. 2, pp. 827–829, 1991.

[72] T. Lu and N. Fleck, "The thermal shock resistance of solids," *Acta materialia*, vol. 46, no. 13, pp. 4755–4768, 1998.

[73] D. S. Kiefer, "Reactive ion etch recipes for failure analysis," *Microelectronic Failure Analysis. Desk Reference, 3 rd Edition. ASM International, Member/Customer Service Center, Materials Park, OH 44073-0002, USA, 1993.*, pp. 125–131, 1993.

[74] W. Baerg, V. Rao, and R. Livengood, "Selective removal of dielectrics from integrated circuits for electron beam probing," in *30th International Reliability Physics Symposium*, 1992.